ADVANCED FUNCTIONAL MATERIALS
www.afm-journal.de

Microscopy of Graphene Growth, Processing, and Properties

Peter Sutter and Eli Sutter*

The growth and properties of two-dimensional (2D) materials–graphene as well as related monolayer systems, such as hexagonal boron nitride–on metals are topics of high scientific and technological interest. Real-time low-energy electron microscopy (LEEM) can provide unique insight into the fundamental growth mechanisms of 2D materials on metal substrates. In combination with in situ spectroscopic measurements, LEEM can greatly facilitate the search for synthesis and processing protocols that produce 2D materials with desired properties for applications. Here, progress is reviewed in understanding the scalable growth of high-quality graphene on metals, novel processing strategies based on selective chemical reactions at the graphene/metal interface, and important materials properties (structure, electronic properties, work function, etc.) by surface microscopy and complementary methods, using graphene/ruthenium as a model system. The body of work shows that in situ microscopy can be used as a powerful tool for achieving and probing a wide range of functionalities in 2D materials.

1. Introduction

Graphene has been used to explore the fascinating properties of ideal two-dimensional (2D) sp^2 bonded carbon, and owing to its extreme electronic, mechanical, and chemical characteristics graphene shows great promise for applications in micro- or nanoelectronics,[1,2] nanomechanics,[3] sensing,[4] chemically inert coatings,[5,6] as well as a host of novel, less conventional uses such as reflective optics for neutral atoms and molecules.[7] The original method for isolating graphene, micromechanical cleavage of graphite,[8,9] can produce mono- and few-layer graphene with exceptionally high charge carrier mobility showing unique transport and magneto-transport properties,[10–12] very low defect density and exceptional mechanical strength,[13] but its scale-up for the mass production of wafer-scale batches of graphene with uniform properties poses almost insurmountable challenges.

Epitaxial growth is an attractive alternative and has been pursued actively on SiC(0001),[14] inspired by earlier work on SiC graphitization dating back several decades.[15] The use of a semi-insulating substrate such as SiC can be particularly advantageous for the fabrication of graphene-based devices, e.g., for high-speed electronics and radio-frequency applications.[16] However, the carrier mobilities achieved even with optimized growth processes, which give rise to relatively large (several 10 μm) graphene domains with minimal (±1 layer) thickness fluctuations have remained far below those of exfoliated graphene, raising concerns about possible fundamental limitations due to intrinsic scattering centers at the graphene-SiC interface,[17] and pointing to the need for scalable processes for synthesizing transferable graphene. Epitaxy on metals provides such a process but has not been considered seriously at first, despite a string of surface studies of 'monolayer graphite' on metals such as Ni,[18], Pt,[19] as well as metal carbides (e.g., TiC, TaC[20]) since the early 1980s. Interest in graphene growth on transition metals has spiked following a report, based primarily on real-time surface imaging by low-energy electron microscopy (LEEM), of facile graphene growth in macroscopic domains and with very high crystal quality by carbon surface segregation on Ru(0001).[21] Alternative approaches, principally the synthesis of transferable graphene by hydrocarbon chemical vapor deposition (CVD) on thin films or foils of non-noble transition metals (e.g., Ni,[22,23] Cu[24]) that are easily etched away to release the graphene for transfer to arbitrary supports, have followed in rapid succession. Meanwhile, further LEEM investigations of graphene growth on Ru(0001) single crystals and more recently epitaxial Ru thin films,[25,26] complemented by similar studies on other metals, such as Pt(111),[27] have demonstrated the unique combination of favorable characteristics of this particular system for large-scale synthesis of very high quality graphene for applications, and have provided fundamental insight into the interaction of graphene with transition metals as well as novel processing approaches aimed at tuning the graphene-metal interface.

Here, we review the rich set of phenomena exposed by cathode lens microscopy[28,29] (LEEM, PEEM) experiments that are relevant for practical applications or are of fundamental interest, including the competition between different carbon supplies in growth processes on metal single crystals and thin films, the scalable growth of few-layer graphene with controlled thickness, the graphene-metal interfacial interaction, and the modification of the graphene-metal coupling by adding graphene layers or by intercalation and chemical modification of the metal surface beneath a graphene sheet. Finally, we show

Dr. P. Sutter, Dr. E. Sutter
Center for Functional Nanomaterials
Brookhaven National Laboratory
Upton, NY 11973, USA
E-mail: psutter@bnl.gov

DOI: 10.1002/adfm.201203426

that relatively simple modifications of metal surfaces by graphitic carbon and other species (e.g., oxygen) can be used to achieve nanometer-scale variations of the local surface potential, important for adjusting the local work function for optimal charge transfer in contacts to photovoltaic or nanoelectronic devices.

2. Graphene Growth

A viable technology for the large-scale production of graphene has to fulfill a number of important practical requirements (**Figure 1**). These include the use of a suitable substrate that is either sufficiently inexpensive or recyclable, and available in large sizes either in the form of wafers, thin films, or foils; and a growth process, such as chemical vapor deposition (CVD), which is readily scaled up to large substrate sizes. The graphene produced by such a process should contain a very low density of both point defects and extended defects comparable to the highest-quality exfoliated material. Ideally, the chosen substrate should have a crystalline surface mesh that provides a lattice-matched template for graphene epitaxy. In this case, assuming a conventional scenario of nucleation and growth, graphene domains that nucleate independently on the substrate surface will be in registry with one another both in lateral spacing and azimuthal orientation, i.e., can eventually coalesce to a continuous, defect-free layer.

This ideal case is realized very rarely, and most substrates considered to date have a significant lattice mismatch with respect to the graphene mesh. Given the extraordinary stiffness of the graphene lattice, this misfit is not (as in ordinary strained-layer heteroepitaxy[30]) accommodated by straining the layer up to a critical thickness and introduction of dislocations thereafter. Instead, the growing graphene sheet adopts a moiré structure, i.e., it remains nearly unstrained and forms a higher-order commensurate structure (typically a n×n/(n+1)×(n+1) coincidence lattice) with the underlying substrate.[31–34] A graphene layer growing in such a moiré structure is invariably polycrystalline, and even if all nuclei share the same in-plane orientation, neighboring grains (or domains) are likely out of registry due to a finite in-plane shift.[35] In fact, for a n×n coincidence lattice there are n^2 different possible nucleation

Peter Sutter is a scientist and Leader of the "Interface Science & Catalysis" group in the Center for Functional Nanomaterials at Brookhaven National Laboratory. He received M.Sc. and Ph.D. degrees in Physics from ETH Zürich. His research focuses on surface physics & chemistry, 2D materials, and nanocatalysis for energy conversion and storage.

Eli Sutter is a scientist in the Center for Functional Nanomaterials at Brookhaven National Laboratory. She received M.Sc. and Ph.D. degrees in Condensed Matter Physics from Sofia University. Her research focuses on in situ transmission electron microscopy studies of properties of nanoscale objects, mechanisms of self-assembly of 2D materials, nanowires and heterostructures.

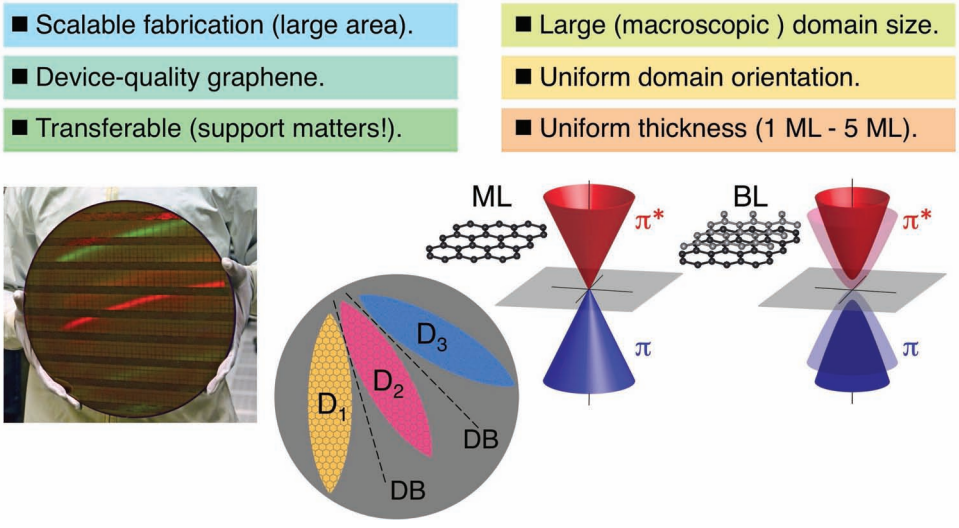

Figure 1. Requirements of a scalable graphene synthesis technology.

geometries, i.e., adjacent domains that nucleate independently from one another are expected to form a line defect upon coalescence in a majority of cases. To minimize the density of these defects, it then becomes necessary to control the growth process so that nucleation is sparse and the individual (monocrystalline) domains are as large as possible.[21] Depending on the strength of the graphene-substrate interaction, the graphene will either be aligned with the substrate lattice (strong coupling) or it can grow in several rotational variants with different in-plane orientation (typical for weak substrate coupling). In the latter case, found for example on Cu and Pt substrates, coalescing domains will be separated by various large-angle boundaries that can have complex atomic arrangements. Assuming that these boundaries are detrimental to the desired properties of the graphene sheet–which is not necessarily the case, e.g., the mechanical strength may actually be increased by domain boundaries[36]—the conclusion is again reached that the domain size should be maximized to minimize the density of line defects.

An issue of particular importance in graphene growth, which has proved to be particularly difficult to achieve, is thickness control. The electronic properties of graphene change significantly with the addition of an individual atomic layer. For example, the bands of monolayer graphene show a linear dispersion near the Fermi energy (characteristic of massless Dirac fermions), whereas the dispersion for bilayer graphene is quadratic (massive Dirac quasiparticles).[37,38] Disorder in the form of thickness fluctuations should therefore significantly affect the transport properties by inducing charge carrier scattering, putting a premium on any growth processes that provide layer-by-layer thickness control. For metal substrates that combine weak graphene-metal interaction and low interstitial carbon solubility (see below), such as Cu,[24] graphene CVD growth essentially stops at a thickness of one layer, since the graphene-terminated metal is highly inert and has a very low dissociative sticking coefficient for typical hydrocarbon growth precursors. While such systems are advantageous for monolayer graphene growth, they are not suitable for the controlled synthesis of bilayer or thicker few-layer graphene.

Finally, most substrates–the semi-insulating SiC being one of the few exceptions–require that the synthesized graphene sheet is isolated and transferred to a support suitable for the chosen application. For non-noble metals, transfer techniques utilizing the stabilization of the graphene film by a deposited polymer layer combined with wet-chemical etching of the sacrificial metal template have been developed[22,23] and optimized to yield transferred graphene without folds and with few additional defects.[39] For noble metals, electrochemical transfer techniques are beginning to emerge,[40] which have the significant advantage of allowing the removal of the graphene sheet without consuming the metal template. Such methods, so far demonstrated only for systems with very weak graphene-metal coupling (e.g., Pt(111)[40]), may enable the use of noble (and costly) metal templates for the growth of transferable, high-quality graphene.

Most graphene growth processes on metals are variants of chemical vapor deposition, and involve the high-temperature exposure of the substrate to a hydrocarbon gas, such as ethylene, methane, or acetylene. The precursor molecules adsorb on the hot transition metal surface, on which they are catalytically dehydrogenated to release carbon atoms onto the surface. The mode in which this carbon eventually assembles into graphene depends on the interstitial carbon solubility in the substrate lattice. In equilibrium at high temperatures, transition metals such as Ru, Re, and Rh can hold moderate amounts (≈1 atomic percent) of carbon in interstitial sites (**Figure 2**a and inset).[41] The C solubility in Ir is about ten times lower and that of Cu is negligible up to the melting temperature. Ni holds much more C, has a complex phase diagram[42] and can form stable surface carbide phases.[43] When a metal with finite interstitial C solubility, such as Ru, is exposed to C at high temperature, the C supply divides into C adatoms and atoms absorbed into interstitial sites, in a ratio that depends primarily on the interstitial C solubility at this temperature. For a sufficiently high supersaturation of C adatoms (e.g., high hydrocarbon gas pressures or long exposures), graphene can directly nucleate and grow by consuming the surface C (surface process, (1) in Figure 2b). In the other extreme, no graphene nucleates during

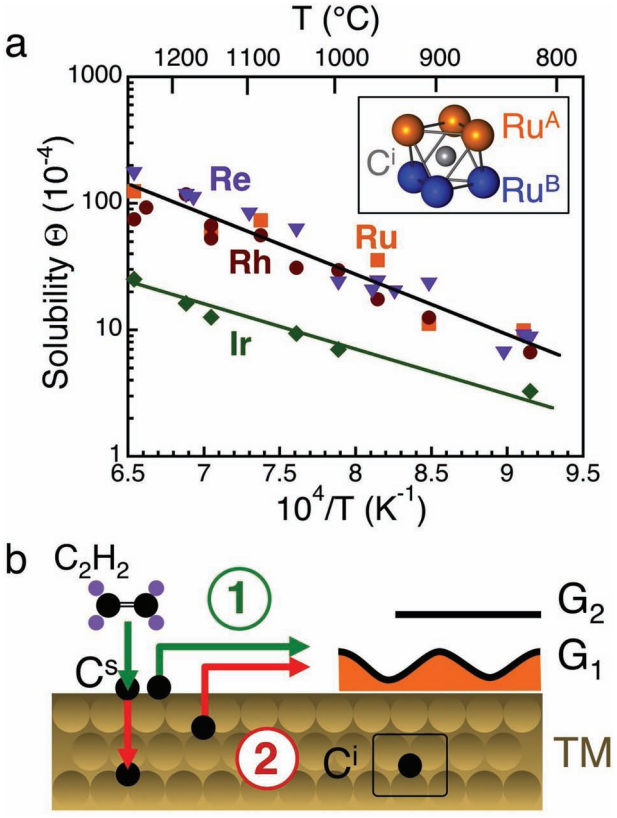

Figure 2. Graphene growth on transition metals. a) Temperature dependent solubility of interstitial carbon in 4d and 5d late transition metals. Inset: Illustration of the octahedral interstitial site in hexagonal-close-packed Ru. b) Graphene growth modes on transition metal substrates exposed to hydrocarbon gas at high temperature: (1) Direct chemical vapor deposition via hydrocarbon dehydrogenation and carbon surface diffusion. (2) Uptake of carbon atoms into interstitial sites, followed by carbon surface segregation and graphene growth upon controlled cooling.

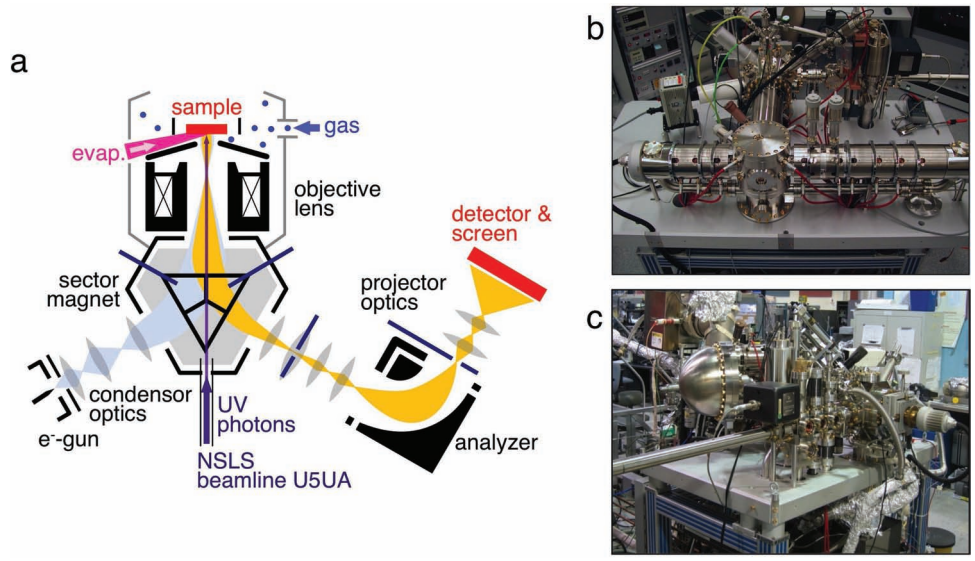

Figure 3. Low-energy electron microscopy (LEEM). a) Schematic beam path in low-energy electron microscopy (LEEM, blue + yellow) and photoelectron microscopy (UV-PEEM, yellow). In LEEM mode a collimated electron beam from a thermal (LaB_6) or field emission source is backscattered and used to obtain an image or diffraction pattern from the sample. In PEEM a high intensity beam of UV photons excites photoelectrons from the sample, which can be used for photoelectron imaging or diffraction. In all operating modes, the sample can be heated or cooled, exposed to gases or vapors from thermal or electron beam evaporator sources. b) Elmitec LEEM V microscope. c) Elmitec LEEM III microscope with imaging energy filter.[46]

hydrocarbon exposure and most liberated C is stored in interstitial sites in the metal. For bulk crystals and thick foils or films, the total amount of interstitial C can readily amount to several graphene monolayers. A controlled temperature decrease causes the reduction of the interstitial C solubility of the metal substrate; the excess C atoms segregate to the surface, add to the adatom population and induce the controlled nucleation and growth of graphene (segregation process, (2) in Figure 2b). In practice, the two processes coexist and both surface C and C segregating from the bulk contribute to graphene growth.

3. Real-Time and Spectroscopic Surface Microscopy: Powerful Tools for Studying Graphene Growth and Properties

Real-time (in situ) microscopy, which has proven to be a powerful tool for studying thin film growth[44] and properties[45] in the past, has dramatically accelerated the understanding of the processes involved in graphene growth. The use of in situ microscopy not only allows the quantitative analysis of nucleation and growth, but it can also provide rapid access to a far larger portion of the growth parameter space than is typically feasible via sequential growth and ex-situ characterization. Most importantly, techniques that allow observations under actual growth conditions (i.e., high temperature, elevated gas pressure, etc.) can detect and analyze complex phenomena that are difficult to identify via the conventional separate growth and characterization, including the possible role of structures that occur only under actual growth conditions.

As part of its signature theme of "in situ/operando microscopy and spectroscopy", the Interface Science and Catalysis group in the Center for Functional Nanomaterials at Brookhaven National Laboratory operates two low-energy electron microscopes (LEEMs) as well as complementary instrumentation for scanning probe microscopy (SPM) and ambient-pressure synchrotron X-ray photoelectron spectroscopy. The two LEEM systems are equipped for real-time observations of graphene growth (**Figure 3**a) and complementary spectroscopic measurements. While a base pressure in the low 10^{-10} torr range provides a controlled environment, CVD growth can be performed at gas pressures up to $\approx 5 \times 10^{-6}$ torr. Other capabilities include thermal and electron beam evaporation for molecular beam epitaxy and the possibility of introducing a variety of reactive gases, enabling the study of processes such as intercalation and etching in real time. Using low-energy electrons for imaging or diffraction, observations can be performed at video rate with high spatial resolution (6–8 nm lateral resolution within a 3 µm field of view), or—often more important for studies on graphene–across a large field of view up to 100 µm (at correspondingly reduced lateral resolution). The vertical resolution is typically 1 atomic layer, and stems either from interference contrast at atomic surface steps or from differences in low-energy electron reflectivity for films of different thickness (e.g., monolayer and bilayer graphene).

A Elmitec LEEM V field-emission microscope (Figure 3b) uses a Schottky field-emission electron gun for high-resolution LEEM and micro-diffraction, and a Hg short-arc lamp as an excitation source for photoelectron emission microscopy (PEEM). A second microscope (Elmitec LEEM III, Figure 3c) equipped with an imaging energy analyzer (energy resolution≈0.2 eV) is operated at beamline U5UA of the National Synchrotron Light Source (NSLS).[46] Exposure to ultraviolet (UV) photons in the energy range from ≈15–150 eV in conjunction with energy filtering enables a host of operation modes in PEEM, including microscopy using valence or shallow core-level photoelectrons,

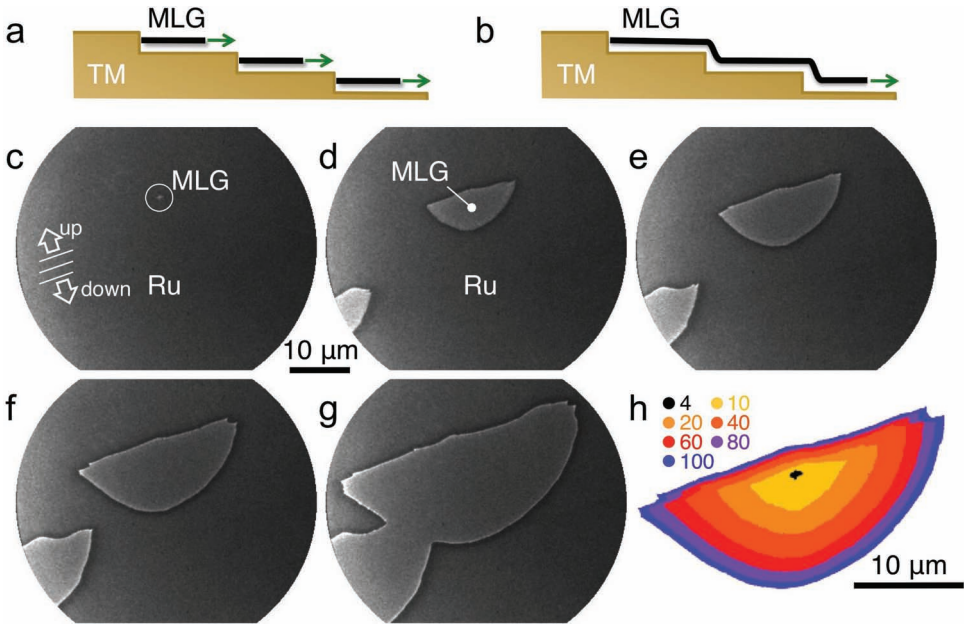

Figure 4. Graphene growth on Ru(0001) during exposure to ethylene at high temperature. Schematics showing a) a possible limited graphene expansion due to strong interaction with surface steps, and b) the coherent, carpet-like flow of monocrystalline graphene domains across substrate steps. c–g) Time-lapse image series of the expansion of a single-crystalline monolayer graphene (MLG) domain via lateral edge-flow due to carbon incorporation. Lines indicate the direction of atomic steps (average spacing: ≈200 nm) on the Ru substrate. Elapsed time after graphene nucleation: 4 s (a); 20 s (b); 40 s (c); 80 s (d); 440 s (e). Temperature: 820 °C, ethylene pressure 8×10^{-9} torr. h) Contours of the graphene domain at different times (in seconds), showing the anisotropic expansion of the domain: rapid growth along atomic terraces and downhill across Ru surface steps, slow growth in the uphill direction across Ru steps.

selected-area angle-resolved photoelectron spectroscopy (micro-ARPES), and local UV or X-ray photoelectron spectroscopy.

4. Real-Time Microscopy of Graphene Growth on Ru(0001)

The real-time imaging of surface processes, such as graphene growth, in direct (LEEM) and reciprocal space (LEED) is one of the well-known applications of cathode lens microscopy. Microscopic observations can be performed with high (≈100 ms) temporal resolution under actual growth conditions, and the results can be analyzed quantitatively to extract important characteristics such as the growth rates of individual 2D nuclei, the rate of expansion in different directions on the surface, the concentration of surface carbon atoms, etc. Hence, such studies are powerful in providing a quantitative understanding of graphene growth.

Aside from the different modes of carbon supply discussed above, and the specific incorporation mechanism of carbon atoms into the graphene edge,[47] the interaction with surface steps is a key aspect of the growth of graphene comprising macroscopic monocrystalline domains on metal substrates, such as Ru(0001).[21] A clean, well-defined metal surface consists of atomically flat terraces separated by monolayer high steps. Typical step separations fall into the range between ≈10–200 nm. Since surface steps represent low-coordinated sites and are distinctly more reactive than terrace sites, the interaction with substrate steps could limit the ultimate size of graphene domains on metals (**Figure 4**a), thus causing a high density of graphene domain boundaries comparable to the step density of the substrate. Instead, LEEM observations of the nucleation and growth on Ru substrates have demonstrated that monocrystalline graphene domains can grow coherently across substrate steps (Figure 4b),[21] which enables the growth of graphene layers consisting of macroscopic domains with lateral sizes of tens or even hundreds of μm. However, even though the interaction with steps is sufficiently weak to allow monocrystalline graphene domains to extend across many substrate steps, real-time microscopy shows that the interaction with Ru steps cannot be neglected entirely, but causes anisotropic growth rates along different in-plane directions (Figure 4c–g) and gives the graphene nuclei their characteristic lens-shaped appearance. Following the initial nucleation, which appears to occur generally at step-sites (Figure 4c),[33] the graphene domain extends rapidly along steps and across steps in the downhill direction. While not completely suppressed, growth across steps in the uphill direction is significantly slower (Figure 4h). This slow uphill step crossing has been explained by pinning of the graphene edge by undercoordinated step atoms.[21] Monolayer graphene interacts with a flat metal substrate primarily through hybridization of the out-of-plane π orbitals with metal d bands, while in-plane σ states participate in sp^2 bonding. This picture breaks down when a graphene edge meets a substrate step. The lattice orientation of graphene on Ru(0001) implies that a zigzag graphene edge with

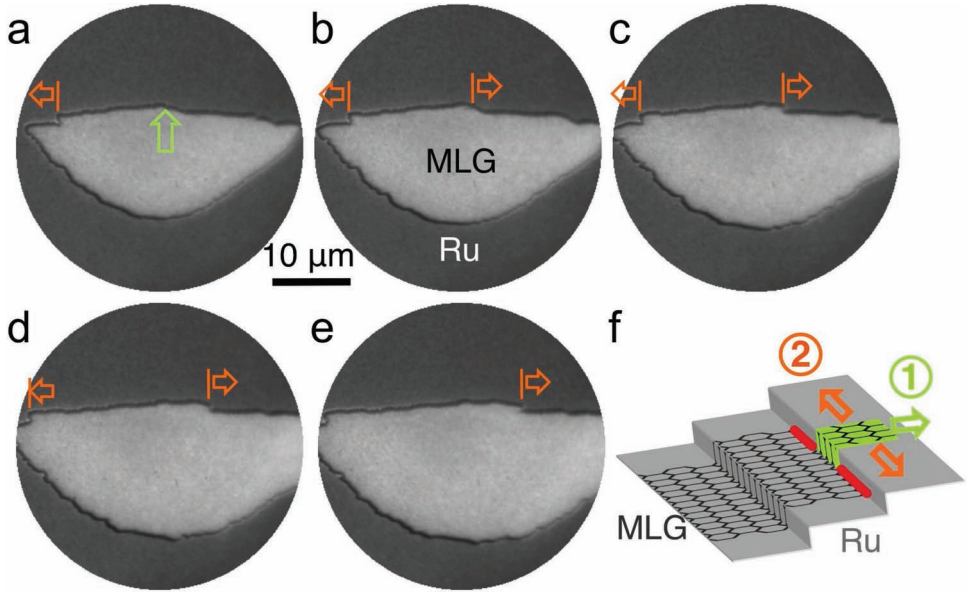

Figure 5. Mode of the slow graphene growth uphill across Ru surface steps. a–e) Time-lapse image series of the expansion of a single-crystalline monolayer graphene (MLG) domain via lateral edge-flow due to carbon incorporation. Elapsed time (relative to (a)): 30 s (b); 40 s (c); 50 s (d); 60 s (e). f) Schematic showing the uphill expansion of the domain across Ru steps. The graphene zigzag edge projected toward the step is pinned at the step (red lines). (1) Spontaneous local unpinning of the graphene edge; (2) Lateral graphene expansion along the upper terrace.

localized dangling σ bonds[48] is projected onto atomic substrate steps. A graphene boundary encountering an uphill step maximizes the orbital overlap and becomes immobilized at the step edge. Conversely, a graphene sheet growing in the "downhill" direction shows minimal overlap of the edge states with the Ru step, and can flow uninhibited in a carpet-like fashion across the step. This growth mode results in macroscopic graphene domains reaching hundreds of μm in size, far larger than the substrate step spacing.[21]

The fast growth along atomic terraces and downhill across steps can be understood by the facile incorporation of small carbon clusters into the graphene edge, which leads to a nearly continuous expansion by edge attachment. The residual, very slow growth in the uphill direction involves a more complex mechanism that can be identified from real-time LEEM image sequences on Ru surfaces prepared to contain bunches of multiple steps (**Figure 5**a–e). While largely suppressed, spontaneous uphill step crossing of the graphene is observed in small sections of the pinned edge. Once the edge has crossed the step it can rapidly extend further until it becomes pinned by the next step. The subsequent growth occurs along the upper terrace until it is fully covered by graphene. This two-step unpinning and growth mechanism is illustrated schematically in Figure 5f. Growth on other metals, such as Pt,[27] Ir,[49] or Cu[50] does not involve the pronounced anisotropy in the graphene growth rate observed here for Ru(0001), but instead shows nearly isotropic growth rates and strongly faceted graphene domains. This difference in the growth and shape of graphene nuclei is a first indication of a strong interfacial interaction between a graphene monolayer and the Ru substrate, in contrast to the much weaker coupling of graphene to other metal substrates. Several other graphene properties that are governed by this coupling to the Ru substrate will be discussed in greater detail below.

As the individual graphene domains expand laterally, they ultimately coalesce (as shown in the early stages in Figure 4g) to form a complete graphene monolayer. The ability to grow few-layer graphene beyond the initial atomic layer depends on the growth mode employed. Studies using low-pressure ($< 10^{-6}$ torr) hydrocarbon exposures of Ru thin films, which provide a negligible reservoir for interstitial carbon, have shown that CVD growth by a surface mechanism alone self-terminates with the completion of a monolayer graphene sheet.[26] A similar self-termination is observed for example on Cu[24] and Ir,[49] which have either negligible or low carbon solubility at typical graphene growth temperatures. CVD growth on Cu at higher pressures leads to minority areas that exceed monolayer thickness, but this type of growth is seen as a parasitic effect and has not been harnessed for controlled few-layer graphene synthesis. Graphene growth by a carbon segregation mechanism can involve amounts of interstitial carbon that are sufficient for forming multiple graphene layers. Indeed, the primary difficulty in graphene growth on metals with high carbon solubility (e.g., Ni) is the uncontrolled carbon segregation during cooling, which typically results in thickness fluctuations of several layers.[22] Alternative growth processes on Ni that suppress this uncontrolled multilayer growth have only recently been identified, but their primary goal has been to offer more control in the synthesis of monolayer graphene.[51,52]

Previous work has shown that in segregation growth on Ru(0001) the first graphene layer can grow to full substrate coverage before the nucleation of a second graphene layer.[17] Real-time LEEM observations have been crucial in exploring the

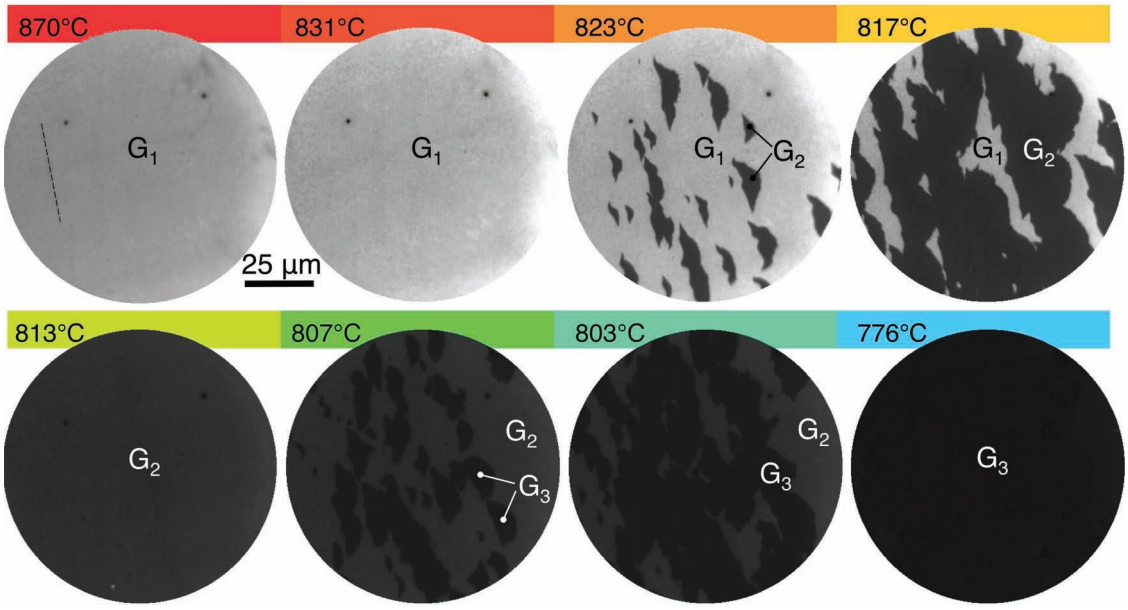

Figure 6. Layer-by-layer graphene growth on Ru(0001) by carbon segregation. Sequence of LEEM images obtained during slow cooling of a carbon-enriched Ru(0001) crystal from about 900 °C. At 870 °C, full substrate coverage of monolayer graphene (G_1) is obtained and retained during further cooling to 830 °C. Further cooling induces the sequential nucleation and growth of a second graphene layer (G_2) up to the completion of a graphene bilayer, followed by the nucleation and growth of a third layer (G_3) up to full substrate coverage of trilayer graphene.

possibility of controlled few-layer graphene growth by carbon segregation on Ru(0001), and the results indicate that a controlled layer-by-layer graphene growth on Ru is indeed feasible (**Figure 6**). Following the uptake of carbon into interstitial sites in the bulk Ru crystal by exposure to ethylene at high temperature (≈1000 °C), the sample is cooled slowly in UHV to induce carbon segregation to the surface. The first graphene layer (G_1) is completed at ≈870 °C. Notably, upon completion of G_1 the temperature can be lowered significantly without any onset of second layer (G_2) nucleation. This observation suggests that a sizable carbon supersaturation near the surface is required to induce the onset of G_2 nucleation. Nucleation eventually takes place at 820 °C, and upon further cooling the G_2 domains grow and coalesce to a complete layer, similar to G_1 previously. Further cooling induces the nucleation, growth, and coalescence of third layer (G_3) domains. However, in contrast to the $G_1 \rightarrow G_2$ transition, only a minimal temperature reduction is necessary to induce G_3 nucleation in the presence of a complete graphene bilayer, pointing to possible differences in the nucleation and growth mode of G_2 and G_3. Overall, these observations show that controlled carbon segregation on bulk Ru(0001) or sufficiently thick Ru films can be used for the scalable layer-by-layer synthesis of few-layer graphene with one to at least three layers thickness.

5. Graphene on Ru(0001): Structure and Substrate Interaction

A strong coupling between graphene and Ru(0001) has been indicated by the anisotropic growth of monolayer graphene domains. The strong interfacial interaction has been confirmed through measurements of other properties of graphene/Ru, such as the electronic band structure (addressed in section 7). Here, we review the consequences of this strong substrate coupling on the structure and morphology of graphene on Ru.

The atomic structure of monolayer graphene/Ru(0001) is shown in **Figure 7**a. LEED (Figure 7b) and STM (Figure 7c) consistently show a moiré structure with about 3 nm repeat distance, in which approximately 12 × 12 unit cells of graphene match 11 × 11 unit cells of the Ru surface mesh. The corrugated monolayer graphene/Ru moiré (Figure 7c) consists of a 'high' or atop region, centered in one half of the unit cell rhombus, where the C atoms occupy fcc and hcp hollow sites relative to surface Ru atoms, and two distinct 'low' areas with (top, hcp) and (top, fcc) registry,[31,34] which provide sites with different reactivity for the adsorption of other species (e.g., metal nanoclusters).[53,54] A careful synchrotron X-ray diffraction study has revealed that the primitive unit cell of the moiré has a periodicity of twice this value.[55] Electron diffraction further shows a fixed relative orientation of the graphene and Ru lattices such that the $\langle 10\bar{1}0 \rangle$ in-plane directions of graphene layer and substrate are aligned with one another. In some experiments small azimuthal misorientations were detected, depending on the preparation conditions.[56] Even so, any boundaries separating coalescing graphene domains will be small-angle boundaries with near zero (few degrees at most) relative misorientation between the adjacent graphene lattices.

The addition of a second graphene layer causes only minor changes in the diffraction pattern (Figure 7d). Importantly, the coincidence lattice between the graphene layer and the substrate stays nearly unchanged. This result implies that the

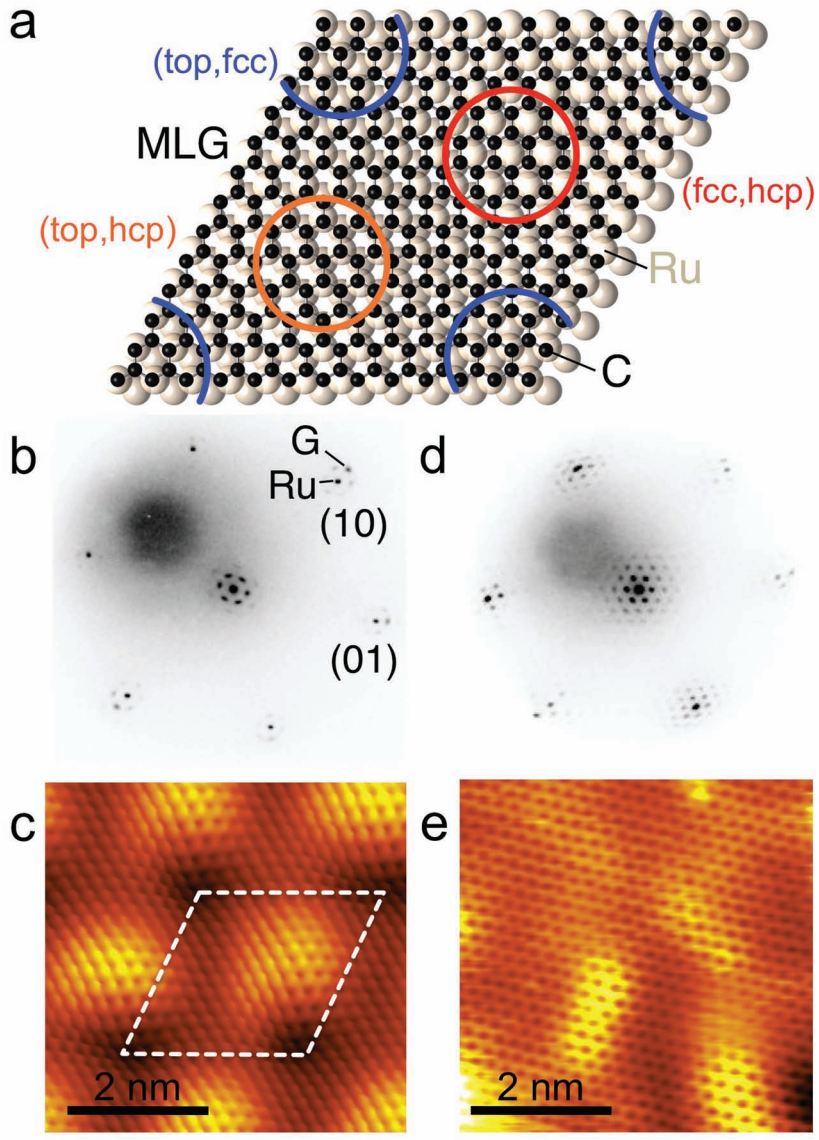

Figure 7. Atomic structure of graphene on Ru(0001). a) Schematic of the monolayer graphene/Ru(0001) moiré structure. The high (fcc, hcp) and the two different low regions of the moiré (with (top, hcp) and (top, fcc) stacking, respectively) are marked. b) Micro-LEED pattern of monolayer graphene on Ru(0001). c) STM image of monolayer graphene/Ru(0001), showing a moiré with ≈3 nm rhombic unit cell. d) Micro-LEED pattern of bilayer graphene on Ru(0001). e) STM image of bilayer graphene/Ru(0001), showing a honeycomb lattice similar to isolated graphene.

second graphene layer has the same in-plane orientation as the first, i.e., the two sheets in bilayer graphene on Ru(0001) are not twisted relative to one another as observed for other systems of graphene on metal (e.g., Ni(111)[57]) and as suggested by calculations for graphene/Ru(0001).[58] LEED intensity-voltage (I-V) characteristics suggest Bernal (A-B) stacking in the bilayer, with an interlayer spacing (3.0 Å) close to that of bulk graphite (3.34 Å).[21] STM of bilayer graphene on Ru(0001) probes primarily the structure of the topmost layer and shows a dramatic change compared to monolayer graphene (Figure 7e). Instead of the mostly triangular lattice with varying registry observed for the complex moiré structure of monolayer graphene, bilayer graphene on Ru(0001) shows a well-resolved honeycomb structure similar to that of exfoliated graphene transferred to SiO_2.[31]

The separation between monolayer graphene and the substrate is clearly the most direct manifestation of the graphene-metal interaction. All measurements and calculations consistently show a strong coupling between monolayer graphene and Ru(0001), which should be manifested by a small separation between the topmost Ru and lowest C atoms, but there is no general agreement in the values for the graphene-metal spacing. The comparison of I-V LEED data with simulations have indicated a very small spacing (1.45 Å), but involved a large uncertainty due to a simplified commensurate model.[21] Density-functional theory suggested a closest separation of 2.2 Å,[34] but may not correctly represent the actual separation because of difficulties in taking into account van der Waals interactions.[59] With the advent of the capability to grow high-quality graphene on Ru thin films on SiO_2/Si,[60] and especially on well-ordered epitaxial Ru(0001) layers on sapphire substrates,[25] a direct measurement of the graphene-metal spacing via cross-sectional transmission electron microscopy could be envisioned.[53] **Figure 8** shows the results of such experiments, analyzed by comparison with dynamic high-resolution TEM image contrast simulations, in which the graphene-metal spacing was varied systematically to obtain an optimal match with experiment. The contrast simulations are necessary because the image interpretation is not straightforward; for example bright spots in the metal layer do not correspond to Ru atoms, but the computed electron density (i.e., atom positions) map shows that they are actually interference fringes between layers of Ru atoms. A best fit between the experimental and simulated images is obtained for a separation between the lowest carbon atoms of the corrugated graphene sheet and the Ru surface of (1.8 ± 0.1) Å, i.e., somewhat lower than suggested by DFT.[53]

6. Growth of High-Quality Transferable Graphene on Epitaxial Ru Films

Robust methods for the scalable fabrication of graphene with macroscopic domain size and uniform thickness are critical to harnessing the unique properties of graphene in applications. Growth on non-carbide forming metal substrates has recently emerged as one of the most promising ways of producing

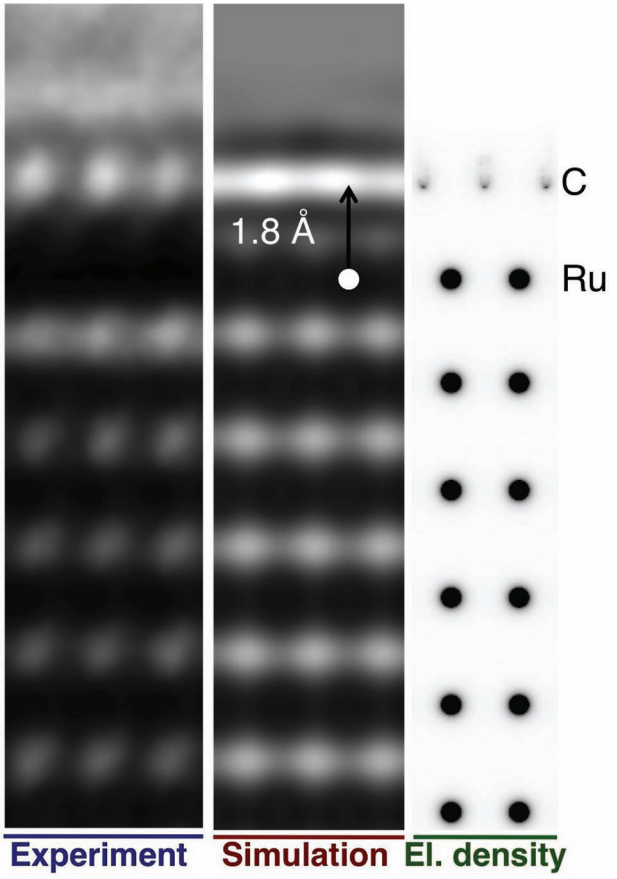

Figure 8. Substrate separation of monolayer graphene on Ru(0001). Left: High-resolution cross-sectional TEM image of monolayer graphene on Ru(0001). Center: Dynamic high-resolution TEM image contrast simulation for a separation of 1.8 Å between the topmost Ru atoms and the lowest-lying carbon atoms in the corrugated graphene moiré.[34] Right: Electron density map, showing the positions of C and Ru atoms. Adapted with permission.[53] Copyright 2011, Elsevier.

high-quality graphene.[21,49] The primary strategy for the synthesis of transferable graphene involves the growth on sacrificial transition metal thin film or foil templates, which ensure the growth of high-quality graphene films but can be etched away to transfer the graphene to a different support. The implementation of this methodology has been demonstrated for Ni,[22,23,61,62] Cu,[63–65] Ru,[5,25,60] and Co[66] substrates.

In addition to the commonly used polycrystalline films and foils, a number of epitaxial transition metal templates for graphene growth have recently been demonstrated, including Ru(0001),[25,67] Ir(111),[68] Cu(111),[69] Ni(111),[67] and Co(111)[67,70] on c-axis sapphire, and Ni(111) on MgO(111).[71] Heterostructures of graphene-terminated epitaxial metal films are beginning to enable new applications, for example graphene on Ru(0001)/Al_2O_3(0001) has recently been demonstrated in high-reflectivity ambient-stable mirrors for neutral atomic beams.[7] Generally, epitaxial thin metal films can have several potential advantages–primarily due to the high template surface quality and absence of grains and grain boundaries in the metal film–compared to polycrystalline graphene growth templates, including: (i) azimuthal alignment (i.e., uniform lattice orientation) of graphene over macroscopic areas; (ii) no areas (e.g., grain boundaries) with preferential carbon segregation; and (iii) uniform metal film thickness, which can then become a design parameter for tailoring graphene growth (**Figure 9**a,b).

Real-time LEEM experiments on ultrathin epitaxial Ru(0001)/Al_2O_3(0001) (Figure 9c) have demonstrated a very low surface roughness comparable to Ru(0001) single crystals and a remarkable thermal stability (up to > 1400 °C), suggesting that it should be possible to translate all of the desirable graphene growth properties identified on single crystals, such as macroscopic domain size, azimuthal alignment, low defect density, etc., to a thin film template from which the graphene can be isolated and transferred to arbitrary supports. Real-time microscopy has demonstrated efficient mechanisms for the removal of oxygen-rich surface contaminants via exposure to a hydrocarbon

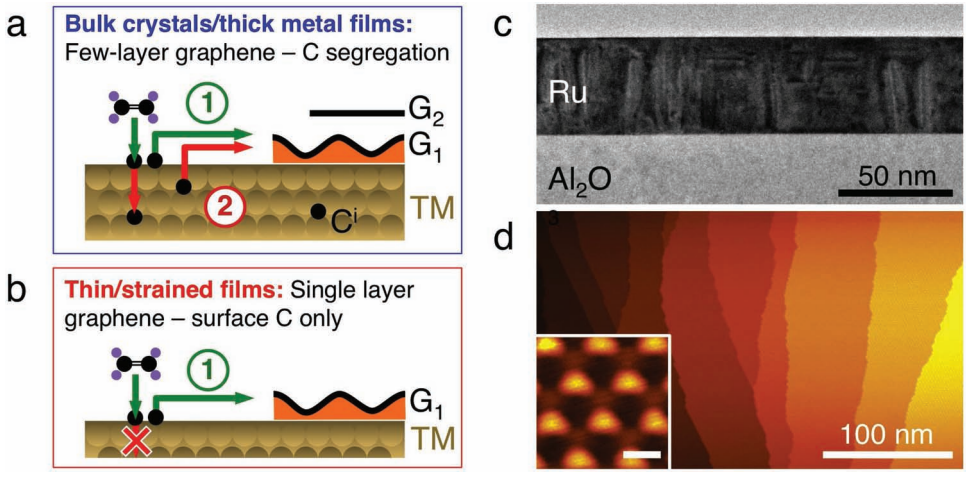

Figure 9. Graphene growth on epitaxial Ru(0001) thin films on c-axis sapphire. a) Schematic showing the growth of few-layer graphene on bulk Ru(0001) or thick Ru films by combined CVD and carbon segregation. b) Schematic showing the suppression of carbon storage in interstitial sites in an ultrathin epitaxial metal film, leading to self-terminating growth of monolayer graphene by CVD alone.[26] c) Cross-sectional TEM image of the epitaxial Ru(0001) graphene growth template on Al_2O_3(0001). d) STM image of a full graphene monolayer on an epitaxial Ru(0001) thin film template. Inset: High-resolution STM image, showing the ordered moiré structure of graphene on the Ru(0001) thin film.

precursor gas, and have proven that large graphene domain sizes and in-plane aligned graphene and Ru lattices are obtained similarly to growth on Ru single crystals.[26] In contrast to single crystals, epitaxial Ru thin films with thickness below 100 nm show very limited carbon uptake into interstitial bulk sites, as may be expected due to the limited Ru thickness and accordingly reduced total carbon storage capacity of the films (Figure 9a,b). LEEM experiments on the dissolution and regrowth of graphene showed carbon uptake even below that expected for a thin film with bulk-like carbon solubility.[26] Elastic lattice strain, identified as the primary reason for the strongly suppressed carbon solubility, can thus be used together with the film thickness to tune the capacity to store and release interstitial carbon in the epitaxial Ru films. The low equilibrium carbon solubility of the thin Ru templates and concomitant suppression of carbon uptake/surface segregation enables the growth by a pure surface process, which self-terminates after the completion of the first layer and thus provides pure monolayer graphene (Figure 9d).

In comparison to other, less noble metal substrates such as Cu and Ni, Ru is significantly more difficult to etch, which complicates the graphene transfer process. Nevertheless, the transfer of graphene grown on epitaxial Ru thin film templates via wet chemical etching of the metal has been demonstrated.[25] Optimization is needed to further reduce the defect density of the transferred graphene, e.g., by using stabilizing polymer layers employed in the transfer from other metal substrates and by identifying etching solutions with enhanced selectivity for Ru. An additional, independent verification of the well-ordered structure and low defect density of graphene grown on epitaxial Ru films is provided by measurements that show the low reactivity (i.e., protection of the metal surface against oxidation) upon exposure to ambient conditions. Thermal He and H scattering on graphene/Ru sandwich structures after long-term (>1 month) exposure to air showed two orders of diffracted beams due to the graphene/Ru moiré structure, suggesting a high-quality, long-range ordered moiré structure equivalent to that on Ru single crystals.[7] The easy recoverability of this clean and highly ordered surface by mild annealing in vacuum demonstrated the perfect surface protection by the graphene layer and a very low overall reactivity of this surface. The combination of this surface passivation with a high specular reflectivity of neutral atomic and molecular beams (23% for He; 7% for H_2) makes this graphene on Ru(0001) thin films promising for applications in atomic and molecular beam optics, for example as surface mirrors for scanning He atom microscopy[72,73] or atomic physics.

7. Electronic Structure of Few-Layer Graphene on Ru(0001)

Beyond the real-time surface imaging and diffraction analysis discussed above, LEEM-based methods can provide a range of complementary measurements to assess functional properties at the nanometer length scale. These methods become particularly powerful if synchrotron radiation is harnessed as an excitation source for photoelectrons. Passing the photoemitted electrons through an energy analyzer opens up the capability to map the electronic band structure analogous to angle-resolved photoelectron spectroscopy (ARPES), but within a small (in our case 2 μm diameter) region of interest on the sample surface, defined by placing an aperture in a virtual image plane of the microscope (selected area or micro-ARPES). This ability to probe the local band structure near surfaces provides a powerful tool to assess the thickness-dependent electronic structure of layer-by-layer synthesized few layer graphene on Ru(0001).

For our LEEM III microscope with imaging energy analyzer, installed at NSLS beamline U5UA,[46] the principle of this micro-APRES measurement is illustrated in **Figure 10** for a sample consisting of a complete graphene monolayer (G_1) on Ru(0001) with additional smaller second-layer nuclei (G_2). Within the real-space LEEM image, a field-limiting aperture is placed to define the region of interest (Figure 10a). With the sample exposed to a focused beam of ultraviolet (UV) synchrotron radiation (photon energy $h\nu = 42$ eV, providing high surface sensitivity), the microscope is switched to diffraction, thus projecting an energy-filtered photoelectron diffraction (PED) pattern onto the detector (Figure 10b). Assuming primarily initial state contributions to the angle-resolved photoelectron intensity, the individual energy-resolved PED intensity patterns correspond to constant-energy cuts through the near-surface band structure. The pass-energy of the analyzer can then be varied incrementally from about -20 eV to Fermi-level to acquire 3D (k_x, k_y, E) maps of the entire band structure (Figure 10c) beyond the first Brillouin zone. In our setup, complete snapshots of the local electronic structure of graphene (–15 eV to 0 eV, 0.1 eV increments) are acquired within about 10 min. From this 3D data set, desired projections, e.g., along high-symmetry directions in reciprocal space, can be computed for analysis and visualization purposes (Figure 10d).

Figure 11 shows the evolution of the electronic structure from monolayer to trilayer graphene on a Ru(0001) substrate. The plots focus on the vicinity of the **K**-point, i.e., the region in reciprocal space in which the linear valence and conduction bands of isolated (undoped) monolayer graphene meet at the charge neutrality point.[38] The electronic structure of the Ru substrate has also been measured and is in good agreement with the calculated projected band structure of clean Ru(0001).[74] The growth of a single graphene layer on Ru(0001) has little effect on the occupied bands near the Fermi energy. Near **K**, it maintains relatively diffuse bands separated by narrow (≈1 eV) gaps, characteristic of the Ru substrate. At higher binding energy (not shown in Figure 11), well-developed π, shifted significantly (2.6 eV) lower in energy compared to free-standing graphene, and weaker σ bands accompany the formation of a graphene monolayer.[75] Importantly, the π-band does not cross the Fermi level, and the characteristic Dirac cones of free-standing monolayer graphene are completely lifted. These characteristics are a direct consequence of the strong coupling between monolayer graphene and the Ru substrate, as suggested by other experimental evidence, such as the close graphene-metal spacing, discussed above. For monolayer graphene on Ru(0001), the same conclusion has been reached by other studies, based on X-ray absorption[76] and angle resolved photoemission[77] experiments, and similar effects of a strong substrate coupling on the electronic band structure have been found for monolayer graphene on Rh(111),[78] Ni(111),[79] and on several transition metal carbides.[20]

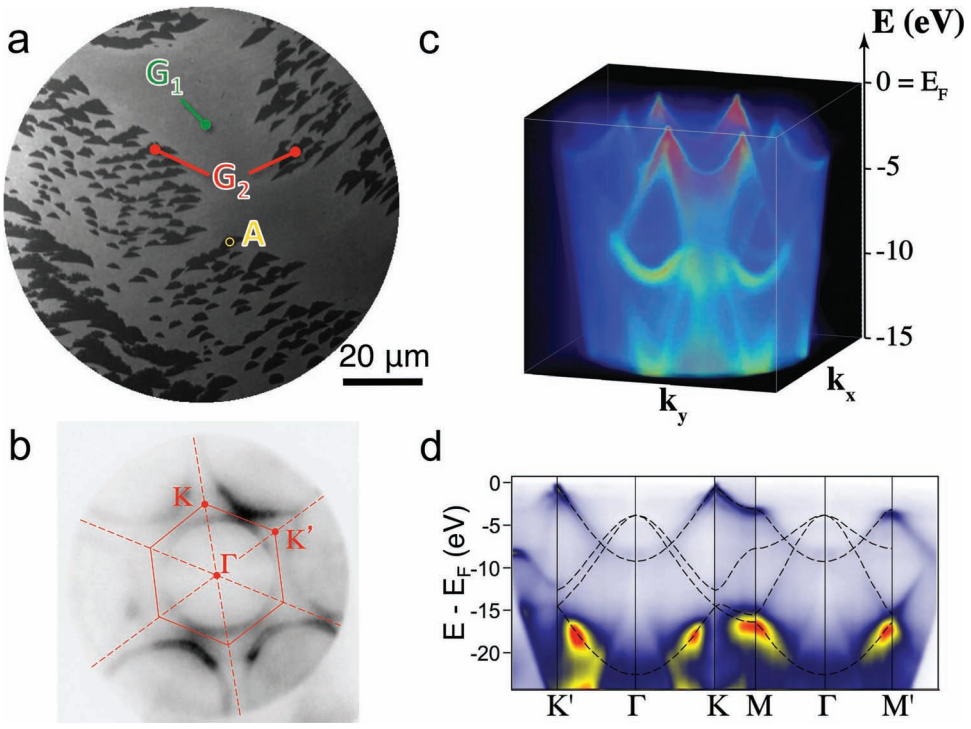

Figure 10. Micro-ARPES measurement by energy-filtered synchrotron PEEM. a) Large-scale LEEM image (100 µm field of view), showing a full graphene monolayer (G_1) and smaller nuclei of a second graphene layer (G_2) on Ru(0001). A yellow circle ('A') shows the size of the field-limiting aperture of the microscope. b) Energy-filtered photoelectron diffraction pattern (energy E = 4.0 eV below the Fermi level), obtained within a 2 µm region of interest in one of the bilayer graphene domains shown in a. c) Full three-dimensional (k_x, k_y, E) band map beyond the first Brillouin zone, assembled from a stack of photoelectron diffraction patterns measured in –0.1 eV energy increments from the Fermi energy. d) Projected band map along the Γ-K and Γ-M directions of the graphene Brillouin zone, derived from the three-dimensional data shown in c. Dashed lines show the bands of free-standing graphene, shifted rigidly by 0.5 eV to lower energy.

Layer-by-layer graphene growth on Ru(0001) beyond the monolayer produces bilayer and finally trilayer graphene. Further micro-ARPES measurements on these few-layer graphene films provide an understanding of the evolution of the band structure with the addition of individual graphene sheets.[75] The transition from monolayer to bilayer graphene leads to particularly pronounced changes in the electronic structure (Figure 11). A narrow, intense π-band of the outer layer, whose width is limited by the resolution of the energy analyzer, now crosses the Fermi level (E_F). The bilayer shows π-bands with linear dispersion that closely match the calculated tight-binding bands of free-standing graphene,[80] except for a shift to lower energy due to residual electron doping by the adjacent metal (E_D = -0.5 eV). The Fermi velocity of $(1.0 \pm 0.1) \times 10^6$ m/s, deduced from the linear π-band dispersion is in excellent agreement with the electron group velocity in exfoliated graphene.[81] Overall, bilayer graphene on Ru recovers the signature of massless Dirac fermions characteristic of isolated *monolayer* graphene.

A micro-ARPES map of trilayer graphene shows a band structure close to that expected for massive Dirac fermions in free-standing *bilayer* graphene (Figure 11). The π-bands of the trilayer appear much broader, with a splitting (0.4 eV)[82] due to the interlayer interaction resolved near **K**, and closely match the pair of parabolic bands computed for an isolated graphene bilayer using an approximate Hamiltonian[83] valid near K, with smaller electron doping E_D = -0.30 eV and band velocity v = 1.05×10^6 m/s.

The evolution of the band structure of few-layer graphene on Ru is strikingly similar to that of epitaxial graphene on SiC,[83,84] for which an interfacial "buffer layer"—strongly coupled to the SiC substrate and without linear π-bands crossing E_F is followed by a two-layer sandwich that recovers the Dirac cones of monolayer graphene (with nearly identical electron doping as found on Ru). The micro-ARPES measurements for monolayer and bilayer graphene on Ru further corroborate conclusions from Raman spectroscopy. Raman spectra of monolayer graphene on Ru show a weak G band, but the double-resonant 2D Raman line[85] is absent. A narrow 2D band appears in bilayer graphene on Ru,[21] confirming that the outer sheet of bilayer epitaxial graphene/Ru(0001) has essentially the electronic structure of free-standing monolayer graphene.

It is instructive to compare these results for graphene on Ru(0001) to other graphene-metal systems. In contrast to the strong interfacial coupling of graphene on Ru(0001)[75] and Rh(111),[86] the 5d late transition metals have generally shown much weaker interfacial interactions.[78] Graphene growth on Pt(111) results in a multitude of rotational graphene domains, which show a large separation to the underlying metal surface consistent with a weak van der Waals coupling. Micro-ARPES measurements confirm this picture, showing well-defined Dirac

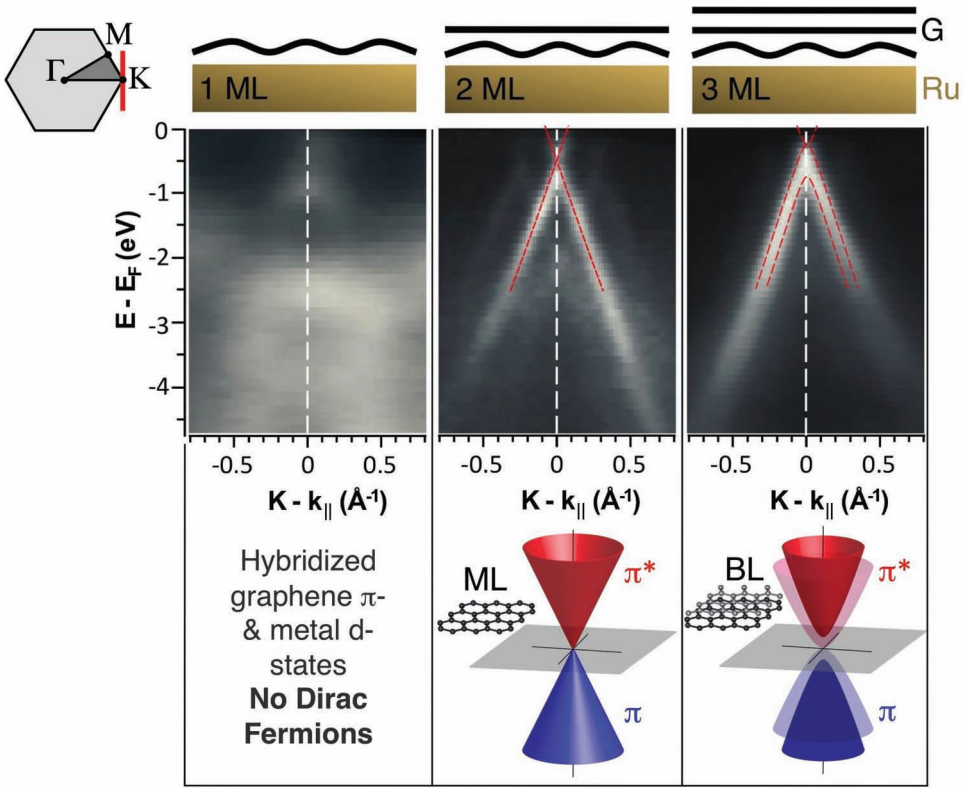

Figure 11. Electronic structure of graphene/Ru(0001). Micro-ARPES band maps of 1, 2, and 3 layer graphene films on Ru(0001), measured through the K-point in a direction perpendicular to Γ-K (inset, red line).

cones and a minimal charge transfer (hole) doping already for monolayer graphene on Pt(111).[27] Similarly, a nearly preserved band structure, which is only minimally affected by the metal susbstrate, has been demonstrated for graphene on Ir(111).[87] A very weak interaction would be expected for graphene supported on Au(111), but the direct growth on this surface by CVD is very challenging due to the low reactivity of Au surfaces. A recent report has shown that physical vapor deposition (i.e., carbon evaporation) can be used to grow graphene on Au(111).[88] Similar to Pt and Ir, this system shows at least two possible graphene domain orientations, as well as slight hole doping due to charge transfer from the Au surface.

8. Chemistry Under Cover: Tuning the Graphene-Metal Interaction

The strong graphene-metal interaction manifested through the small interfacial spacing and perhaps most directly via the measurements of the band structure makes monolayer graphene on Ru an interesting model system for studying interfacial processes that could modify and possibly weaken the interaction. A general approach for decoupling the graphene from the metal can be developed if species are found that will react preferentially with the metal surface beneath an intact graphene sheet. Oxygen represents such a species, but similar behavior can be expected for a wide range of atomic and molecular adsorbates that bind more strongly to Ru than to defect-free graphene and thus experience a thermodynamic driving force for migrating to the graphene-metal interface. The conditions of exposure to such reactive species need to be considered carefully due to the possibility of unwanted "side-reactions"–in the case of oxygen, for example, the combustion reaction to CO_2 or CO–with the graphene, and particularly with low-coordinated sites such as point defects, graphene edges, etc.

O_2 adsorption on clean Ru(0001) is dissociative, initially with a sticking coefficient near unity. At low O_2 pressures, it gives rise to a progression of ordered O-adlayer structures beginning with a p(2 × 2)-O structure[90] that is completed at 0.25 ML coverage, and followed by a p(2 × 1)-O structure at 0.5 ML coverage (**Figure 12**a).[91] At this point, the O_2 sticking coefficient drops sharply, causing an apparent saturation of adsorption under low-pressure conditions. Oxygen binds very strongly to Ru(0001), with a binding energy per atom much larger than that for monolayer graphene on Ru(0001) (Figure 12b), suggesting that there should be a strong thermodynamic driving force for oxygen–terminating the metal surface beneath graphene. The reactivity of the graphene surface to oxygen is much lower than that of the metal and penetration of atoms and molecules even through a single graphene monolayer is nearly completely suppressed, as demonstrated by the fact that graphene-termination of metal surfaces (e.g., Ni(111),[92] Fe/Ni(111),[93] Ru(0001),[5,7] Cu and Cu alloys[6]) can be used as an atomically thin but still very efficient coating to prevent the oxidation of metal surfaces during exposure to ambient air.

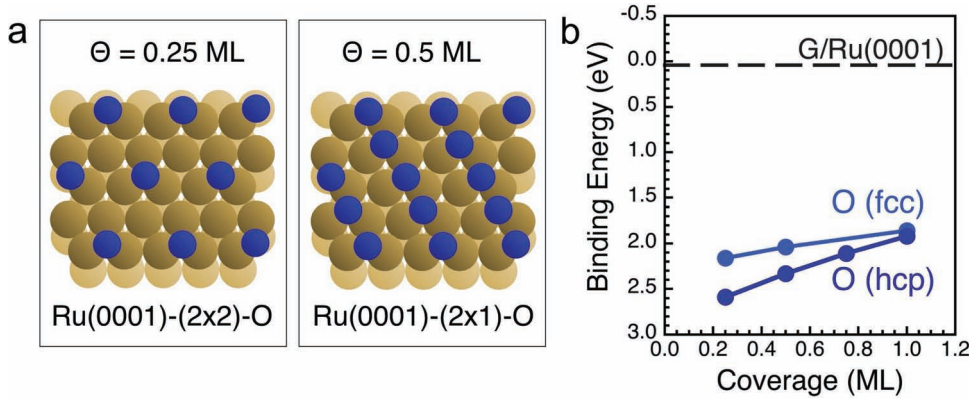

Figure 12. O-adlayer reconstructions induced by oxygen adsorption on Ru(0001). a) (2×2)-O and (2×1)-O superstructures at oxygen coverages $\Theta = 0.25$ ML and $\Theta = 0.5$ ML, respectively. b) Coverage dependent binding energy per O atom of adsorbed oxygen in fcc and hcp sites on Ru(0001) (after ref.[89]), and comparison with the binding energy (per carbon atom) of monolayer graphene (G) on the Ru(0001) surface.[34]

Figure 13a shows a LEEM image series obtained during the exposure of a Ru(0001) surface–partially covered by large monolayer graphene domains–to molecular oxygen ($p(O_2) = 5 \times 10^{-7}$ torr) at slightly elevated temperature (T = 280 °C). Dissociative O_2 adsorption gives rise to a rapid change in image contrast in the exposed (i.e., not graphene-covered) Ru surface areas, which is followed by a slower penetration of oxygen beneath the graphene sheets, i.e., along the graphene-metal interface. This interfacial intercalation of oxygen continues until the entire Ru surface beneath the graphene sheets is terminated by an ordered oxygen adlayer structure, as shown by clear half-order diffraction spots detected in LEED behind the reaction front.[94]

Micro-ARPES measurements, performed on both sides of the reaction front, provide direct evidence of the effects of reactive oxygen intercalation and O-termination of the Ru surface on the electronic structure of the graphene layer (Figure 13b). Band maps of the as-grown graphene strongly coupled to Ru are consistent with the findings discussed above, i.e., are dominated by the hybridization of the graphene π-bands with metal d-states and do not show the characteristic Dirac cones of free-standing graphene (Figure 13c). Measurements behind the intercalation front, i.e., in areas in which the Ru surface has been modified by oxygen-intercalation and formation of an ordered oxygen adlayer structure, show dramatically different results (Figure 13d). Here, the electronic bands represent a superposition of the Ru(0001) projected band structure with additional, narrow bands consistent with nearly isolated graphene. In particular, well-developed σ-bands and π-bands with

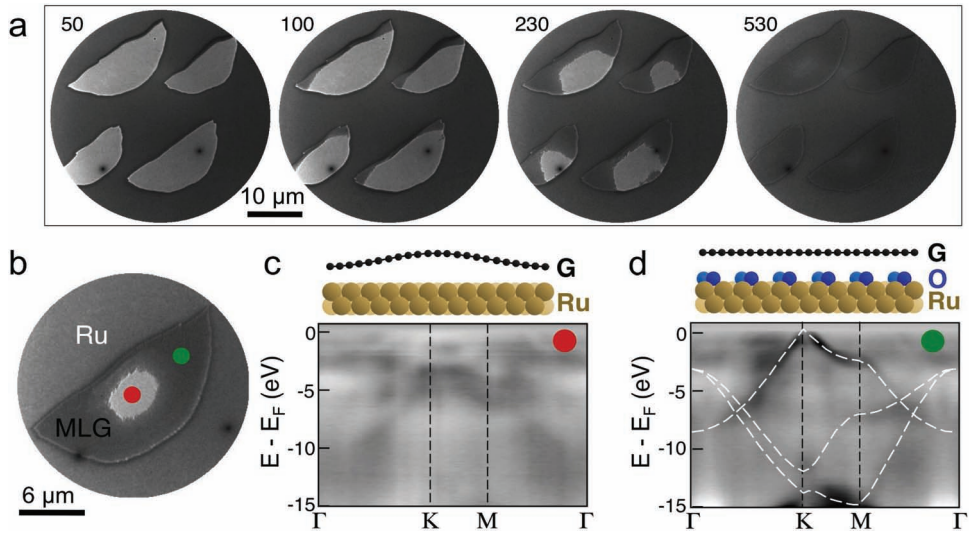

Figure 13. Decoupling of graphene on Ru(0001) by oxygen intercalation. a–LEEM image series of a Ru(0001) surface partially covered with large graphene domains during exposure to molecular oxygen ($p(O_2) = 5 \times 10^{-7}$ torr; T = 280 °C). Exposure times (in seconds) are given in the individual panels. b) LEEM image of a partially oxygen-intercalated monolayer graphene domain on Ru(0001). c,d) Micro-ARPES band maps of c) as-grown (red dot in b) and d) oxygen intercalated graphene (green dot in b), showing the electronic decoupling of the graphene accompanying the formation of an ordered oxygen adlayer structure on the Ru surface beneath the graphene sheet.

linear dispersion are recovered near the Fermi energy in the vicinity of the K-point of the surface Brillouin zone. Instead of the electron doping observed for the top sheets of bilayer and trilayer graphene on Ru, the decoupling by oxygen-terminating the Ru surface causes hole doping due to charge transfer to the strong electron acceptors at the interface, shifting the charge neutrality point by 0.5 eV above the Fermi level.

One of the particularly powerful capabilities of LEEM is the relative ease of performing observations at different temperatures to gain insight on reaction kinetics. An Arrhenius analysis of the temperature dependent oxygen intercalation rate determined by such measurements has provided insight into the kinetics of the selective reaction of oxygen with the Ru surface beneath graphene, and has clarified the demarcation between the intercalation/decoupling at low temperature and the combustion of graphene, which takes place at high temperatures.[94]

These spectroscopic microscopy experiments on oxygen intercalation and metal oxidation beneath intact graphene are relevant in two contexts: (i) chemical reactions on surfaces in the presence of graphitic carbon; and (ii) the development of novel processing strategies for graphene on metals. The finding that chemical reactions can proceed in a controlled way on metal surfaces beneath graphene contrasts with the long-held notion that graphitic carbon acts as a poison that suppresses desired chemical reactions in surface chemistry and catalysis. Importantly, the graphene sheet does not merely act as a passive spectator, but it can provide two types of novel functionality. It generates a confined reaction space that precludes the access of large species, and may allow even small molecules to enter only if they adopt particular "low-profile" orientations. Apart from such confinement effects, there is already evidence that the proximity of a graphene sheet can modify important other reaction parameters, such as adsorption energies of reactants.[94] Interfacial chemistry has the potential to become a foundation for novel processing strategies for graphene, in particular to achieve the electrical decoupling and isolation of graphene from a metal growth substrate without requiring any transfer from the metal. For example, simultaneous or sequential intercalation and reaction of multiple species (e.g., Si, O) at the graphene-metal interface can be used to form an interfacial layer that may serve as a gate dielectric, with the underlying metal remaining in place and acting as a gate electrode. Recent work has shown progress toward the realization of this vision. Silicon intercalation has been demonstrated for graphene on Ru(0001), and caused a decoupling qualitatively similar to that obtained with oxygen but with residual electron doping.[95] Via this process, whose mechanism remains unclear and requires further investigation, Si layers with 1 ML and 2 ML thickness could be fabricated between graphene and the metal surface, suggesting that the formation of thicker semiconducting and insulating interfacial layers may be feasible. A demonstration of the additional reaction with O_2 to create, via the oxidation of an intermediate Ru-silicide, an interfacial dielectric SiO_2 layer has been reported recently,[96] supporting the notion that intercalation and interfacial reactions can provide a general approach for engineering functional interfacial layers between a graphene sheet and a metal substrate.

9. Graphene and Oxygen Induced Work Function Changes on Ru(0001)

The injection or extraction of charge carriers between a contact and an active layer is a fundamental process that lies at the heart of a multitude of technologies, including inorganic and organic photovoltaics,[97,98] solid-state light emitters, and nanoelectronics.[99] Optimizing these charge transfer processes requires contacts whose work function (φ^{Cont}) is tailored relative to the work function of the active region (φ^{S}) to allow facile electron ($\varphi^{Cont} < \varphi^{S}$) or hole injection ($\varphi^{Cont} > \varphi^{S}$).[100] Identifying materials that fulfill these conditions, and are both stable under ambient conditions and do not react with the material of the active layer can be challenging. Even more difficult is the engineering of systems in which regions with high and low *local* work function[101] (or surface potential) coexist in close proximity, so as to provide electron- and hole injecting contacts for active device elements such as carbon nanotubes or semiconductor nanowires, whose characteristic dimensions are at the nanoscale. Finally, as important as these materials challenges is the development of versatile, quantitative measurement methods capable of determining the local surface potential with high spatial resolution.

To date, scanning probe techniques such as Kelvin probe force microscopy[102,103] have been the methods of choice for measuring and mapping laterally varying surface potentials, but these approaches are often slow, require controlled ambient conditions and sample surfaces that are stable and do not change over time. LEEM offers the possibility of observing the processing of samples that provide nanoscale work function contrast, and mapping the local potential with high spatial and energy resolution. Indeed, such measurements can easily be performed at variable temperature and during exposure to reactive species (gases, atomic- or molecular beams) that may dynamically alter the work function.

The principle of local work function measurements in cathode lens microscopy has been known since the late 1970s.[104] It utilizes the transition between mirror electron microscopy (MEM) and LEEM, as the sample potential is increased relative to that of the electron gun cathode (**Figure 14**a). In MEM the turning point of the (classical) trajectories of the imaging electron beam lies in front of the sample, giving a very high reflectivity approaching unity; in LEEM, the imaging electron beam strikes and interacts with the sample. Hence–virtually independent of the sample material–the MEM-LEEM transition involves a sharp drop in backscattered intensity.[104] The sample potential, V, at which this intensity drop occurs,[105] $e \cdot V = \varphi^{S} - \varphi^{C}$ (Figure 14a,b) can be measured with very high spectral (≈few meV) resolution and with the full spatial resolution of the microscope. It is important to note that this procedure gives the local work function of the sample (φ^{S}) relative to the work function of the cathode (φ^{C}). An absolute determination of φ^{S} requires an additional measurement of the work function φ^{C} of the electron emitter, e.g., via a reference sample with known work function. In this way, the local surface potential can be determined rapidly even at high temperatures or during processing of the surface. The only limitation of this technique arises in samples with large, abrupt potential changes. In such cases, the resulting in-plane electric fields

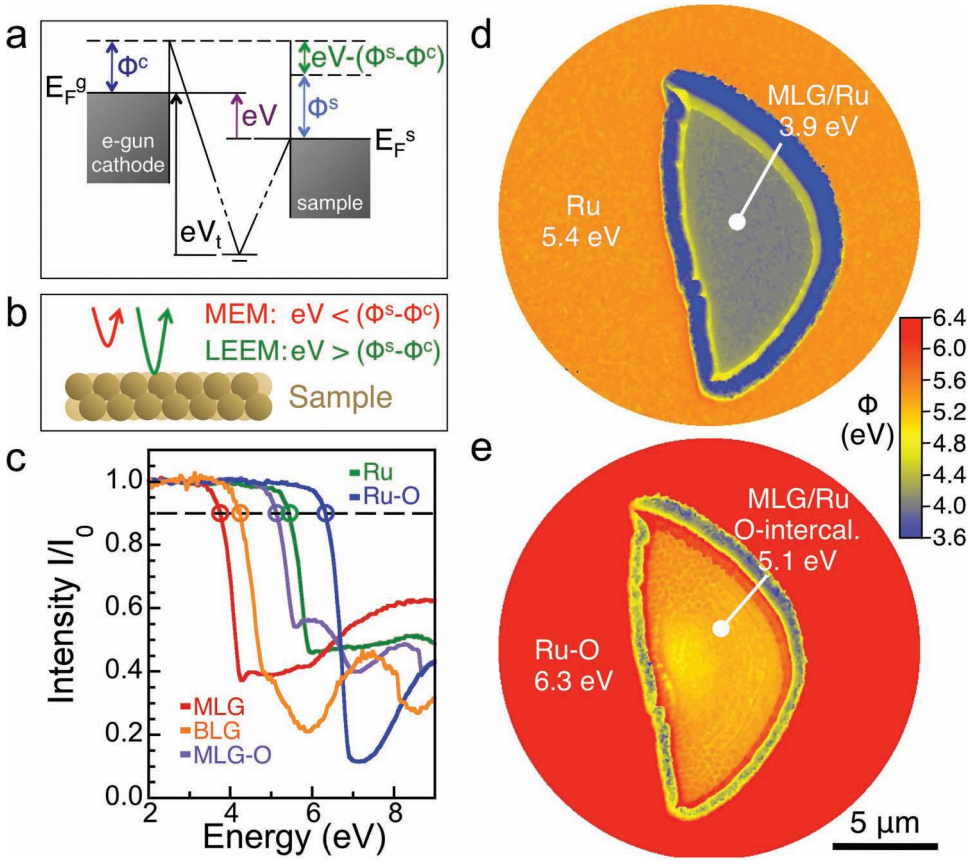

Figure 14. Ru work function tuning by graphene growth, oxygen exposure and intercalation. a,b) Schematic diagrams illustrating the measurement of local surface potentials (i.e., sample work functions, φ^S) in LEEM. For applied sample potential ("start voltage") $V < (\varphi^S - \varphi^C)/e$, electrons are reflected in front of the surface (mirror electron microscopy, MEM) with high, nearly constant reflected intensity, I_0. For $V < (\varphi^S - \varphi^C)/e$, the transition to LEEM leads to a sharp drop in reflected intensity, which can serve to measure the local surface potential, φ^S (given a known/calibrated work function φ^C of the electron gun cathode). c) Measurements of the work function of different graphene and oxygen-modified Ru(0001) surfaces, demonstrating the wide range of work functions (3.9 eV–6.4 eV) accessible in this system. d,e) High-resolution maps of the local surface potential, obtained by detection of the local MEM-LEEM transition.

deflect the imaging electrons and create a finite transition zone in which the measurement breaks down.

Ru(0001) surfaces modified by graphene growth or oxygen adsorption/intercalation provide a very large span of local work functions (from ≈3.9 eV to >6 eV), and hence constitute a materials system that lends itself well to tailoring local work functions (e.g., for applications in nanoelectronics) by relatively simple processing, as well as an interesting model to demonstrate the power of LEEM-based local surface potential mapping. LEEM measurements of the work functions of larger (µm sized) uniform regions with different surface termination are shown in Figure 14c. Starting with clean Ru(0001) (φ^S = 5.45 eV), which also serves as the reference sample, the work function drops dramatically with the growth of a graphene monolayer on Ru. The measured φ^S = 3.90 eV for monolayer graphene on Ru is consistent with values obtained for this system by photoelectron spectroscopy,[106] and confirms the formation of an interfacial dipole involving charge transfer between the graphene layer and the metal surface.[107] Given a reduced electrostatic band shift for the top sheet of bilayer graphene on Ru as determined by micro-ARPES, an increase in the work function to bring it closer to that of graphite (4.60 eV[108]) would be expected, similar to results for few-layer graphene on SiC,[109,110] and is indeed confirmed (φ^S = 4.25 eV). Given the observation of an inversion of doping (from electron to hole-doping) induced by oxygen-intercalation of graphene on Ru, oxygen exposure should continue the trend to higher work function. Local measurements within intercalated graphene domains give φ^S = 5.12 eV, close to the work function of clean Ru(0001). The surfaces with highest work functions in the (Ru, C, O) system have been obtained by oxygen exposure of clean Ru. For example, φ^S = 6.35 eV is measured on the Ru surface adjacent to an oxygen intercalated graphene domain. Similar LEEM-based work function measurements have been reported for graphene on SiC[109] and on Pd,[111] where small changes in surface potential were found for coexisting rotational domains. Besides epitaxial graphene, similar methods can be applied to measure the work function of other surface systems, as illustrated by recent work on surface characterization of icosahedral Al-Pd-Mn quasi-crystals.[112]

The work function measurement illustrated in Figure 14a–c can be performed in every pixel of a LEEM image by *locally* determining the sample potential at which the MEM-LEEM transition occurs, thus producing high-resolution work function maps of inhomogeneous surfaces. Since the measurement is quite fast, such data sets can even be acquired during sample processing. An example of this capability is illustrated in Figure 14d,e, which show maps of the same graphene domain on Ru(0001) directly after graphene growth (Figure 14d), and following an additional process of low-temperature O_2 exposure and oxygen intercalation (Figure 14e). After graphene growth, the graphene domain uniformly shows $\varphi^{MLG} = 3.9$ eV, whereas the surrounding Ru surface remains at $\varphi^{Ru} = 5.4$ eV, despite an increased concentration of thermal carbon adatoms in equilibrium with graphene.[47] The transition region at the graphene boundary, in which strong in-plane electric field components due to the high work function contrast preclude the measurement, is easily observed. O_2 exposure rapidly increases the work function of the metal, and the work function of the graphene domain via oxygen intercalation shows a sharp rise behind the well-defined intercalation front. At the end of this process the entire domain has $\varphi^{S} > 5$ eV, but in contrast to the pristine graphene domain it shows measurable variations—e.g., a lower work function in the central region that was intercalated last–which can be attributed to different local O-coverage.

10. Beyond Graphene: Synthesis of 2D Materials and Heterostructures

This review has focused primarily on graphene/Ru(0001) to illustrate the growth, processing, and properties within this system and to discuss the use of in situ microscopy methods–primarily cathode lens microscopy, i.e., LEEM and PEEM–for studying graphene on metals. Similar microscopy methods have been used to study graphene on other supports, notably other metals and SiC. Besides graphene, other 2D crystals have received increasing attention recently. Similar to graphene, harnessing the properties of materials, such as hexagonal boron nitride (h-BN) or molybdenum disulfide (MoS_2), in large-scale applications will require the identification of growth protocols and processing conditions tailored to their unique physical and chemical properties. In situ and real-time microscopy methods, as discussed here in relation to graphene, can be expected to make important contributions to these studies on other 2D materials systems. As an example, real-time LEEM observations have been used recently to identify conditions for the CVD growth of monolayer h-BN by exposure to borazine at high temperature, which produce films consisting of macroscopic monocrystalline domains.[113] The quantitative analysis of coverage-dependent growth rates in LEEM movies has demonstrated the important role of the extremely low reactivity of h-BN and the effects caused by adding reactive gases (e.g., H_2) to the growth precursor in the CVD process.[113]

Finally, in situ microscopy can play a crucial role in identifying approaches for preparing more complex engineered materials, in which different 2D sheets are either stacked atomic layer-by-layer on top of each other or are joined in a single monolayer membrane. Particularly the synthesis of heterostructured 2D membranes with well-defined interfaces presents unique challenges, and raises fundamental questions on materials integration, such as interface formation, intermixing, strain, polarity, etc. in a new context at reduced dimensionality. Graphene and boron nitride are an attractive pair of materials that can be integrated to form 2D heterostructures in individual monolayer membranes.[114,115] A first study on the controlled formation of graphene/h-BN monolayer heteromembranes by sequential hydrocarbon (ethylene) and borazine CVD on Ru(0001) has depended heavily on the unique microscopy and analytical capabilities of LEEM to identify process conditions that produce atomically sharp 1D graphene/h-BN interfaces.[116] BN attaches preferentially to existing graphene domains and does not produce any secondary nuclei at high temperature, which is consistent with the preferential incorporation of boron and nitrogen at the graphene edge. However, substantial intermixing in the form of carbon doping of the growing h-BN was found near the line interface. Analytical LEEM experiments, capable of quantitatively tracking the concentration of carbon adatoms on Ru(0001),[47] identified carbon monomers on the metal surface as the primary source of this doping and allowed the development of methods for eliminating this carbon reservoir. The findings of these in situ experiments enabled the synthesis of single-membrane graphene/h-BN heterostructures with atomically sharp boundaries, paving the way for exploring the unusual electronic propoerties such as half-metallicity[117] and interfacial electronic correlations[118] predicted for these heterostructures.

Acknowledgements

This research has been carried out at the Center for Functional Nanomaterials, Brookhaven National Laboratory, which is supported by the U.S. Department of Energy, Office of Basic Energy Sciences, under Contract No. DE-AC02-98CH10886. The authors gratefully acknowledge contributions to this research by postdocs and collaborators, including D. P. Acharya, P. Albrecht, M. Batzill, M.-L. Bocquet, R. Cortes, J. I. Flege, M. Hybertsen, F. Ivars-Barcelo, K. Kisslinger, E. Koren, J. Lahiri, G. Nazin, G. Nintzel, J. T. Sadowski, E. Vescovo, B. Wang, L. J. Wu, P. Zahl, and Y. Zhu.

Received: November 21, 2012
Revised: February 28, 2013
Published online: April 11, 2013

[1] Y. M. Lin, C. Dimitrakopoulos, K. A. Jenkins, D. B. Farmer, H. Y. Chiu, A. Grill, P. Avouris, *Science* **2010**, *327*, 662.
[2] L. Britnell, R. V. Gorbachev, R. Jalil, B. D. Belle, F. Schedin, A. Mishchenko, T. Georgiou, M. I. Katsnelson, L. Eaves, S. V. Morozov, N. M. R. Peres, J. Leist, A. K. Geim, K. S. Novoselov, L. A. Ponomarenko, *Science* **2012**, *335*, 947.
[3] C. Chen, S. Rosenblatt, K. I. Bolotin, W. Kalb, P. Kim, I. Kymissis, H. L. Stormer, T. F. Heinz, J. Hone, *Nat. Nanotechnol.* **2009**, *4*, 861.
[4] F. Schedin, A. K. Geim, S. V. Morozov, E. W. Hill, P. Blake, M. I. Katsnelson, K. S. Novoselov, *Nat. Mater.* **2007**, *6*, 652.
[5] E. Sutter, P. Albrecht, F. E. Camino, P. Sutter, *Carbon* **2010**, *48*, 4414.
[6] S. Chen, L. Brown, M. Levendorf, W. Cai, S.-Y. Ju, J. Edgeworth, X. Li, C. W. Magnuson, A. Velamakanni, R. D. Piner, J. Kang, J. Park, R. S. Ruoff, *ACS Nano* **2011**, *5*, 1321.

[7] P. Sutter, M. Minniti, P. Albrecht, D. Farias, R. Miranda, E. Sutter, *Appl. Phys. Lett.* **2011**, *99*, 211907.
[8] K. S. Novoselov, A. K. Geim, S. V. Morozov, D. Jiang, Y. Zhang, S. V. Dubonos, I. V. Grigorieva, A. A. Firsov, *Science* **2004**, *306*, 666.
[9] K. S. Novoselov, D. Jiang, F. Schedin, T. J. Booth, V. V. Khotkevich, S. V. Morozov, A. K. Geim, *Proc. Natl. Acad. Sci. USA* **2005**, *102*, 10451.
[10] K. I. Bolotin, K. J. Sikes, Z. Jiang, M. Klima, G. Fudenberg, J. Hone, P. Kim, H. L. Stormer, *Solid State Commun.* **2008**, *146*, 351.
[11] K. I. Bolotin, K. J. Sikes, J. Hone, H. L. Stormer, P. Kim, *Phys. Rev. Lett.* **2008**, *101*, 096802.
[12] G. Nazin, Y. Zhang, L. Zhang, E. Sutter, P. Sutter, *Nat. Phys.* **2010**, *6*, 870.
[13] C. Lee, X. Wei, J. W. Kysar, J. Hone, *Science* **2008**, *321*, 385.
[14] K. V. Emtsev, A. Bostwick, K. Horn, J. Jobst, G. L. Kellogg, L. Ley, J. L. McChesney, T. Ohta, S. A. Reshanov, J. Rohrl, E. Rotenberg, A. K. Schmid, D. Waldmann, H. B. Weber, T. Seyller, *Nat. Mater.* **2009**, *8*, 203.
[15] D. V. Badami, *Nature* **1962**, *193*, 570.
[16] P. Avouris, *Nano Lett.* **2010**, *10*, 4285.
[17] P. Sutter, *Nat. Mater.* **2009**, *8*, 171.
[18] R. Rosei, S. Modesti, F. Sette, C. Quaresima, A. Savoia, P. Perfetti, *Phys. Rev. B* **1984**, *29*, 3416.
[19] B. Lang, *Surf. Sci.* **1975**, *53*, 317.
[20] C. Oshima, A. Nagashima, *J. Phys: Condens. Matter* **1997**, *9*, 1.
[21] P. W. Sutter, J.-I. Flege, E. A. Sutter, *Nat. Mater.* **2008**, *7*, 406.
[22] A. Reina, X. Jia, J. Ho, D. Nezich, H. Son, V. Bulovic, M. S. Dresselhaus, J. Kong, *Nano Lett.* **2009**, *9*, 30.
[23] K. S. Kim, Y. Zhao, H. Jang, S. Y. Lee, J. M. Kim, K. S. Kim, J.-H. Ahn, P. Kim, J.-Y. Choi, B. H. Hong, *Nature* **2009**, *457*, 706.
[24] X. Li, W. Cai, J. An, S. Kim, J. Nah, D. Yang, R. Piner, A. Velamakanni, I. Jung, E. Tutuc, S. K. Banerjee, L. Colombo, R. S. Ruoff, *Science* **2009**, *324*, 1312.
[25] P. W. Sutter, P. M. Albrecht, E. A. Sutter, *Appl. Phys. Lett.* **2010**, *97*, 213101.
[26] P. Sutter, C. V. Ciobanu, E. Sutter, *Small* **2012**, *8*, 2250.
[27] P. Sutter, J. T. Sadowski, E. Sutter, *Phys. Rev. B* **2009**, *80*, 245411.
[28] E. Bauer, *Surf. Rev. Lett.* **1998**, *05*, 1275.
[29] T. Schmidt, S. Heun, J. Slezak, J. Diaz, K. C. Prince, G. Lilienkamp, E. Bauer, *Surf. Rev. Lett* **1998**, *05*, 1287.
[30] E. A. Fitzgerald, *Mater. Sci. Rep.* **1991**, *7*, 87.
[31] E. A. Sutter, D. P. Acharya, J. T. Sadowski, P. W. Sutter, *Appl. Phys. Lett.* **2009**, *94*, 133101.
[32] A. T. N'Diaye, S. Bleikamp, P. J. Feibelman, T. Michely, *Phys. Rev. Lett.* **2006**, *97*, 215501.
[33] S. Marchini, S. Gunther, J. Wintterlin, *Phys. Rev. B* **2007**, *76*, 075429.
[34] B. Wang, M.-L. Bocquet, S. Marchini, S. Günther, J. Wintterlin, *Phys. Chem. Chem. Phys.* **2008**, *10*, 3530.
[35] G. Dong, E. B. Fourre, F. C. Tabak, J. W. M. Frenken, *Phys. Rev. Lett.* **2010**, *104*, 096102.
[36] R. Grantab, V. B. Shenoy, R. S. Ruoff, *Science* **2010**, *330*, 946.
[37] K. S. Novoselov, A. K. Geim, S. V. Morozov, D. Jiang, M. I. Katsnelson, I. V. Grigorieva, S. V. Dubonos, A. A. Firsov, *Nature* **2005**, *438*, 197.
[38] A. H. Castro Neto, F. Guinea, N. M. R. Peres, K. S. Novoselov, A. K. Geim, *Rev. Mod. Phys.* **2009**, *81*, 109.
[39] X. Li, Y. Zhu, W. Cai, M. Borysiak, B. Han, D. Chen, R. D. Piner, L. Colombo, R. S. Ruoff, *Nano Lett.* **2009**, *9*, 4359.
[40] L. Gao, W. Ren, H. Xu, L. Jin, Z. Wang, T. Ma, L.-P. Ma, Z. Zhang, Q. Fu, L.-M. Peng, X. Bao, H.-M. Cheng, *Nat. Commun.* **2012**, *3*, 699.
[41] W. J. Arnoult, R. B. McLellan, *Scr. Metall.* **1972**, *6*, 1013.
[42] A. A. Vertman, N. A. Nedumov, A. M. Samarin, *Dokl. Akad. Nauk SSSR* **1965**, *162*, 1304.
[43] J. Lahiri, T. Miller, L. Adamska, I. I. Oleynik, M. Batzill, *Nano Lett.* **2010**, *11*, 518.
[44] P. Sutter, M. G. Lagally, *Phys. Rev. Lett.* **2000**, *84*, 4637.
[45] P. Sutter, M. G. Lagally, *Phys. Rev. Lett.* **1999**, *82*, 1490.
[46] J. I. Flege, E. Vescovo, G. Nintzel, L. H. Lewis, S. Hulbert, P. Sutter, *Nucl. Instrum. Methods* **2007**, *261*, 855.
[47] E. Loginova, N. C. Bartelt, P. J. Feibelman, K. F. McCarty, *New J. Phys.* **2008**, *10*, 093026.
[48] K. Nakada, M. Fujita, G. Dresselhaus, M. S. Dresselhaus, *Phys. Rev. B* **1996**, *54*, 17954.
[49] J. Coraux, A. T. N'Diaye, M. Engler, C. Busse, D. Wall, N. Buckanie, F. J. Meyer zu Heringdorf, R. van Gastel, B. Poelsema, T. Michely, *New J. Phys.* **2009**, *11*, 023006.
[50] Q. Yu, L. A. Jauregui, W. Wu, R. Colby, J. Tian, Z. Su, H. Cao, Z. Liu, D. Pandey, D. Wei, T. F. Chung, P. Peng, N. P. Guisinger, E. A. Stach, J. Bao, S.-S. Pei, Y. P. Chen, *Nat. Mater.* **2011**, *10*, 443.
[51] R. S. Weatherup, B. C. Bayer, R. Blume, C. Ducati, C. Baehtz, R. Schlögl, S. Hofmann, *Nano Lett.* **2011**, *11*, 4154.
[52] R. Addou, A. Dahal, P. Sutter, M. Batzill, *Appl. Phys. Lett.* **2012**, *100*, 021601.
[53] E. Sutter, P. Albrecht, B. Wang, M. L. Bocquet, L. J. Wu, Y. M. Zhu, P. Sutter, *Surf. Sci.* **2011**, *605*, 1676.
[54] E. Sutter, B. Wang, P. Albrecht, J. Lahiri, M.-L. Bocquet, P. Sutter, *J. Phys: Condens. Matter* **2012**, *24*, 314201.
[55] D. Martoccia, P. R. Willmott, T. Brugger, M. Bjorck, S. Gunther, C. M. Schleputz, A. Cervellino, S. A. Pauli, B. D. Patterson, S. Marchini, J. Wintterlin, W. Moritz, T. Greber, *Phys. Rev. Lett.* **2008**, *101*, 126102.
[56] K. L. Man, M. S. Altman, *Phys. Rev. B* **2011**, *84*, 235415.
[57] A. Dahal, R. Addou, P. Sutter, M. Batzill, *Appl. Phys. Lett.* **2012**, *100*, 241602.
[58] B. Wang, M.-L. Bocquet, *Nanoscale* **2012**, *4*, 4687.
[59] W. Kohn, Y. Meir, D. E. Makarov, *Phys. Rev. Lett.* **1998**, *80*, 4153.
[60] E. Sutter, P. Albrecht, P. Sutter, *Appl. Phys. Lett.* **2009**, *95*, 133109.
[61] Q. Yu, J. Lian, S. Siriponglert, H. Li, Y. P. Chen, S.-S. Pei, *Appl. Phys. Lett.* **2008**, *93*, 113103.
[62] L. G. De Arco, Y. Zhang, A. Kumar, C. Zhou, *IEEE Trans. Nanotechnol.* **2009**, *8*, 135.
[63] X. S. Li, W. W. Cai, J. H. An, S. Kim, J. Nah, D. X. Yang, R. Piner, A. Velamakanni, I. Jung, E. Tutuc, S. K. Banerjee, L. Colombo, R. S. Ruoff, *Science* **2009**, *324*, 1312.
[64] S. Bae, H. Kim, Y. Lee, X. F. Xu, J. S. Park, Y. Zheng, J. Balakrishnan, T. Lei, H. R. Kim, Y. I. Song, Y. J. Kim, K. S. Kim, B. Ozyilmaz, J. H. Ahn, B. H. Hong, S. Iijima, *Nat. Nanotechnol.* **2010**, *5*, 574.
[65] Y. H. Lee, J. H. Lee, *Appl. Phys. Lett.* **2010**, *96*, 083101.
[66] M. E. Ramon, A. Gupta, C. Corbet, D. A. Ferrer, H. C. P. Movva, G. Carpenter, L. Colombo, G. Bourianoff, M. Doczy, D. Akinwande, E. Tutuc, S. K. Banerjee, *ACS Nano* **2011**, *5*, 7198.
[67] S. Yoshii, K. Nozawa, K. Toyoda, N. Matsukawa, A. Odagawa, A. Tsujimura, *Nano Lett.* **2011**, *11*, 2628.
[68] C. Vo Van, A. Kimouche, A. Reserbat-Plantey, O. Fruchart, P. Bayle-Guillemaud, N. Bendiab, J. Coraux, *Appl. Phys. Lett.* **2011**, *98*, 181903.
[69] M. R. Kongara, D. G. Andrew, C. Chun-Hu, M. D. Julie, P. P. Nitin, *Appl. Phys. Lett.* **2010**, *98*, 113117.
[70] H. Ago, Y. Ito, N. Mizuta, K. Yoshida, B. Hu, C. M. Orofeo, M. Tsuji, K.-I. Ikeda, S. Mizuno, *ACS Nano* **2010**, *4*, 7407.
[71] T. Iwasaki, H. J. Park, M. Konuma, D. S. Lee, J. H. Smet, U. Starke, *Nano Lett.* **2011**, *11*, 79.
[72] B. Holst, W. Allison, *Nature* **1997**, *390*, 244.
[73] D. A. Maclaren, B. Holst, D. J. Riley, W. Allison, *Surf. Rev. Lett.* **2003**, *10*, 249.
[74] T. Pelzer, G. Ceballos, F. Zbikowski, B. Willerding, K. Wandelt, U. Thomann, C. Reuß, T. Fauster, J. Braun, *J. Phys.: Condens. Matter* **2000**, *12*, 2193

[75] P. Sutter, M. S. Hybertsen, J. T. Sadowski, E. Sutter, *Nano Lett.* **2009**, *9*, 2654.
[76] A. B. Preobrajenski, M. L. Ng, A. S. Vinogradov, N. Martensson, *Phys. Rev. B* **2008**, *78*, 073401.
[77] T. Brugger, S. Günther, B. Wang, H. Dil, M.-L. Bocquet, J. Osterwalder, J. Wintterlin, T. Greber, *Phys. Rev. B* **2009**, *79*, 045407.
[78] A. B. Preobrajenski, N. May Ling, A. S. Vinogradov, N. Martensson, *Phys. Rev. B* **2008**, *78*, 073401.
[79] A. Varykhalov, J. Sanchez-Barriga, A. M. Shikin, C. Biswas, E. Vescovo, A. Rybkin, D. Marchenko, O. Rader, *Phys. Rev. Lett.* **2008**, *101*, 157601.
[80] S. Reich, J. Maultzsch, C. Thomsen, P. Ordejon, *Phys. Rev. B* **2002**, *66*, 035412.
[81] A. K. Geim, K. S. Novoselov, *Nat. Mater.* **2007**, *6*, 183.
[82] J. C. Charlier, X. Gonze, J. P. Michenaud, *Phys. Rev. B* **1991**, *43*, 4579.
[83] T. Ohta, A. Bostwick, J. L. McChesney, T. Seyller, K. Horn, E. Rotenberg, *Phys. Rev. Lett.* **2007**, *98*, 206802.
[84] T. Ohta, A. Bostwick, T. Seyller, K. Horn, E. Rotenberg, *Science* **2006**, *313*, 951.
[85] A. C. Ferrari, J. C. Meyer, V. Scardaci, C. Casiraghi, M. Lazzeri, F. Mauri, S. Piscanec, D. Jiang, K. S. Novoselov, S. Roth, A. K. Geim, *Phys. Rev. Lett.* **2006**, *97*, 187401.
[86] E. N. Voloshina, Y. S. Dedkov, S. Torbrugge, A. Thissen, M. Fonin, *Appl. Phys. Lett.* **2012**, *100*, 241606.
[87] I. Pletikosic, M. Kralj, P. Pervan, R. Brako, J. Coraux, A. T. N'Diaye, C. Busse, T. Michely, *Phys. Rev. Lett.* **2009**, *102*, 056808.
[88] J. M. Wofford, E. Starodub, A. L. Walter, S. Nie, A. Bostwick, N. C. Bartelt, K. Thürmer, E. Rotenberg, K. F. McCarty, O. D. Dubon, *New J. Phys.* **2012**, *14*, 053008.
[89] C. Stampfl, S. Schwegmann, H. Over, M. Scheffler, G. Ertl, *Phys. Rev. Lett.* **1996**, *77*, 3371.
[90] M. Lindroos, H. Pfnür, G. Held, D. Menzel, *Surf. Sci.* **1989**, *222*, 451.
[91] H. Pfnür, G. Held, M. Lindroos, D. Menzel, *Surf. Sci.* **1989**, *220*, 43.
[92] Y. S. Dedkov, M. Fonin, C. Laubschat, *Appl. Phys. Lett.* **2008**, *92*, 052506.
[93] Y. S. Dedkov, M. Fonin, U. Rudiger, C. Laubschat, *Appl. Phys. Lett.* **2008**, *93*, 022509.
[94] P. Sutter, J. T. Sadowski, E. A. Sutter, *J. Am. Chem. Soc.* **2010**, *132*, 8175.
[95] J. Mao, L. Huang, Y. Pan, M. Gao, J. He, H. Zhou, H. Guo, Y. Tian, Q. Zou, L. Zhang, H. Zhang, Y. Wang, S. Du, X. Zhou, A. H. C. Neto, H.-J. Gao, *Appl. Phys. Lett.* **2012**, *100*, 093101.
[96] S. Lizzit, R. Larciprete, P. Lacovig, M. Dalmiglio, F. Orlando, A. Baraldi, L. Gammelgaard, L. Barreto, M. Bianchi, E. Perkins, P. Hofmann, *Nano Lett.* **2012**, *12*, 4503.
[97] J.-M. Nunzi, *Comptes Rendus Physique* **2002**, *3*, 523.
[98] H. Hoppe, N. S. Sariciftci, *J. Mater. Res.* **2004**, *19*, 1924.
[99] P. Avouris, Z. Chen, V. Perebeinos, *Nat. Nanotechnol.* **2007**, *2*, 605.
[100] Y. Shen, A. R. Hosseini, M. H. Wong, G. G. Malliaras, *ChemPhysChem* **2004**, *5*, 16.
[101] K. Wandelt, *Appl. Surf. Sci.* **1997**, *111*, 1.
[102] M. Nonnenmacher, M. P. O'Boyle, H. K. Wickramasinghe, *Appl. Phys. Lett.* **1991**, *58*, 2921.
[103] W. Melitz, J. Shen, A. C. Kummel, S. Lee, *Surf. Sci. Rep.* **2011**, *66*, 1.
[104] M. Babout, J. C. L. Bosse, J. Lopez, R. Gauthier, C. Guittard, *J. Phys. D: Appl. Phys.* **1977**, *10*, 2331.
[105] Typically, a decrease in reflected intensity to 90% of the intensity in MEM is used to mark the transition point.
[106] T. Brugger, S. Günther, B. Wang, J. H. Dil, M.-L. Bocquet, J. Osterwalder, J. Wintterlin, T. Greber, *Phys. Rev. B* **2009**, *79*, 045407.
[107] B. Wang, S. Günther, J. Wintterlin, M. L. Bocquet, *New J. Phys.* **2010**, *12*, 043041.
[108] K. S. Krishnan, S. C. Jain, *Nature* **1952**, *169*, 702.
[109] H. Hibino, H. Kageshima, M. Kotsugi, F. Maeda, F. Z. Guo, Y. Watanabe, *Phys. Rev. B* **2009**, *79*, 125437.
[110] T. Filleter, K. V. Emtsev, T. Seyller, R. Bennewitz, *Appl. Phys. Lett.* **2008**, *93*, 133117.
[111] Y. Murata, E. Starodub, B. B. Kappes, C. V. Ciobanu, N. C. Bartelt, K. F. McCarty, S. Kodambaka, *Appl. Phys. Lett.* **2010**, *97*, 143114.
[112] B. Unal, Y. Sato, K. F. McCarty, N. C. Bartelt, T. Duden, C. J. Jenks, A. K. Schmid, P. A. Thiel, *J. Vac. Sci. Technol., A* **2009**, *27*, 1249.
[113] P. Sutter, J. Lahiri, P. Albrecht, E. Sutter, *ACS Nano* **2011**, *5*, 7303.
[114] L. Ci, L. Song, C. Jin, D. Jariwala, D. Wu, Y. Li, A. Srivastava, Z. F. Wang, K. Storr, L. Balicas, F. Liu, P. M. Ajayan, *Nat. Mater.* **2010**, *9*, 430.
[115] M. P. Levendorf, C.-J. Kim, L. Brown, P. Y. Huang, R. W. Havener, D. A. Muller, J. Park, *Nature* **2012**, *488*, 627.
[116] P. Sutter, R. Cortes, J. Lahiri, E. Sutter, *Nano Lett.* **2012**, *12*, 4869.
[117] Y.-W. Son, M. L. Cohen, S. G. Louie, *Nature* **2006**, *444*, 347.
[118] J. M. Pruneda, *Phys. Rev. B* **2010**, *81*, 161409.